AIMS Geosciences, 3 (3): 396-437
DOI: 10.3934/geosci.2017.3.396
Received date 02 August 2017
Accepted date 16 August 2017
Published date 21 August 2017

http://www.aimspress.com/journal/geosciences

Research article

Laser Ablation ICPMS Analysis of Pyrite and U-Pb Zircon Dating of Host Rocks From the Tersang Gold Deposit, Malaysia

Charles Makoundi *, Khin Zaw and R.R. Large

ARC Centre of Excellence in Ore Deposits, University of Tasmania

*** Correspondence**: Email: c.makoundi@utas.edu.au; Tel: +61-362262472; Fax: +61-362262547.

Abstract: The Central gold belt of peninsular Malaysia comprises a number of gold deposits located in the east of the N-S striking Bentong-Raub Suture Zone. The Tersang gold deposit is a mesothermal, orogenic gold deposit, which is hosted in sandstone, shale, rhyolite and breccia. The deposit has an inferred and indicated resource of 120,000 ounces of gold in the JORC category. Detrital zircon grains from the host sandstones returned a maximum depositional age ranging from Early Carboniferous to Early Permian (333.5 ± 2.5 Ma-261.5 ± 4.9 Ma) and those of the rhyolite indicated a crystallization age of 218.8 ± 1.7 Ma. Pyrite trace element mapping has revealed four pyrite phases. Laser Ablation ICPMS analyses on pyrite has shown that pyrite phase 1 has the lowest Au concentration (mean 0.4 ppm) and is interpreted to have preceded the main Au mineralisation stage. Pyrite phases 2 and 3 are the main Au mineralisation stage with Au mean range from 1.5 to 4.5 ppm and contributed most of the invisible gold to the ore-forming system. Pyrite phase 4 has low gold concentrations (mean 0.5 ppm) and post-dated the main Au mineralisation stage recorded in pyrite phases 2 and 3. The trace element chemistry of pyrite indicates that Au mineralisation recorded in pyrite is likely a product of four stages ore forming system centred on the rhyolite corridor. In terms of gold exploration, gold has a positive correlation with As, Ag, Cu, Se, Sb, Pb and Tl in pyrite. These metals can be used as pathfinders to detect proximity to ore for orogenic gold deposit type in the central gold belt of Peninsular Malaysia.

Keywords: LA-ICP-MS; Trace element; Pyrite; Tersang gold deposit; Bentong-Raub Suture Zone; Malaysia

1. Introduction

The Tersang gold deposit is located approximately 20 km north of the town of Raub along the eastern side of the Bentong-Raub Suture Zone. Other gold deposits, including Ulu Sokor, Pulai, Chenua, Buffalo Reef, Penjom, Selinsing, and Raub, are also situated in the east of the Bentong-Raub Suture Zone (Figure 1). In 1937, a quantity of 53200 cubic meters of alluvium was mined and about 600 oz of gold were recovered at the mine-site [1]. It is also reported that gold-bearing quartz veins were found in quartz-muscovite rocks in northern Tersang [1]. Peninsular Gold Limited, the current owner of the Tersang gold mine, estimates that the deposit hosts an inferred and indicated resource of 120,000 ounces of gold at 0.71 grams per tonne in the JORC category. It is interpreted that the Carboniferous host rocks of the Tersang gold deposit lie within the Raub Group [2]. The purpose of this study is to constrain depositional ages of host rocks, determine major and trace element composition of the host rocks, document trace element distribution between gold-poor and gold-rich pyrite phase and suggest implications for gold exploration.

2. Geological Setting

Peninsular Malaysia is comprised of three main tectonic terranes/blocks that strike north-south in the Peninsula [2–6]. Yeap [7] defines these terranes as the Western Belt, Central Belt and Eastern Belt after Scrivenor [8] (Figure 1). In recent years, the view that the Malay Peninsula is part of the Southeast Asia continental block which comprises the Sibumasu (Siam, Burma, Malaysia, and Sumatra) Terrane in the west and the Sukhothai Arc (East Malaya Block) in the east has been reiterated [9].

The Western Belt lies within the Sibumasu Terrane. This belt is characterised by Early Palaeozoic continental margin sequences, Late Palaeozoic platform carbonates, Triassic platform carbonates, deep basinal clastic sequences, and Jurassic-Cretaceous continental deposits **(**Figure 1). The Western Tin Belt is associated with the Main Range granitoid province which is a large plutonic belt that extends to the southern Peninsular Thailand and central Thailand [7]. The Central Gold Belt is located in the east of the Bentong-Raub Suture Zone and comprises Permo-Triassic metamorphic rocks, and deep to shallow marine sedimentary rocks [10,11]. The Central Belt also contains limestone with intermediate to felsic volcanic and volcaniclastic rocks (Carboniferous-Triassic in age), which were deposited in a fore-arc portion of the Paleo-arc basin [1,12–14].

The Eastern Belt is part of the East Malaya block and characterised by a poly-deformed Late Palaeozoic sequence, overlain unconformably by Late Permian continental conglomerate and Jurassic-Cretaceous continental deposits. Granitoids in this belt cover a compositional range from biotite granite to hornblende-biotite granite/granodiorite and diorite-gabbro [15]. In addition, this belt includes a suite of shoshonitic trachyte in the Segamat area (Johor) which has been dated by K/Ar dating and returned an age of 62 Ma [16]. The Eastern Belt plutons consist of biotite or hornblende-biotite-bearing I-type granitoids with Triassic Rb-Sr ages. I-type granitoids are typical of modern day Andean-type active margins where oceanic plates are subducted under continental margins or island arcs producing andesite volcanoes.

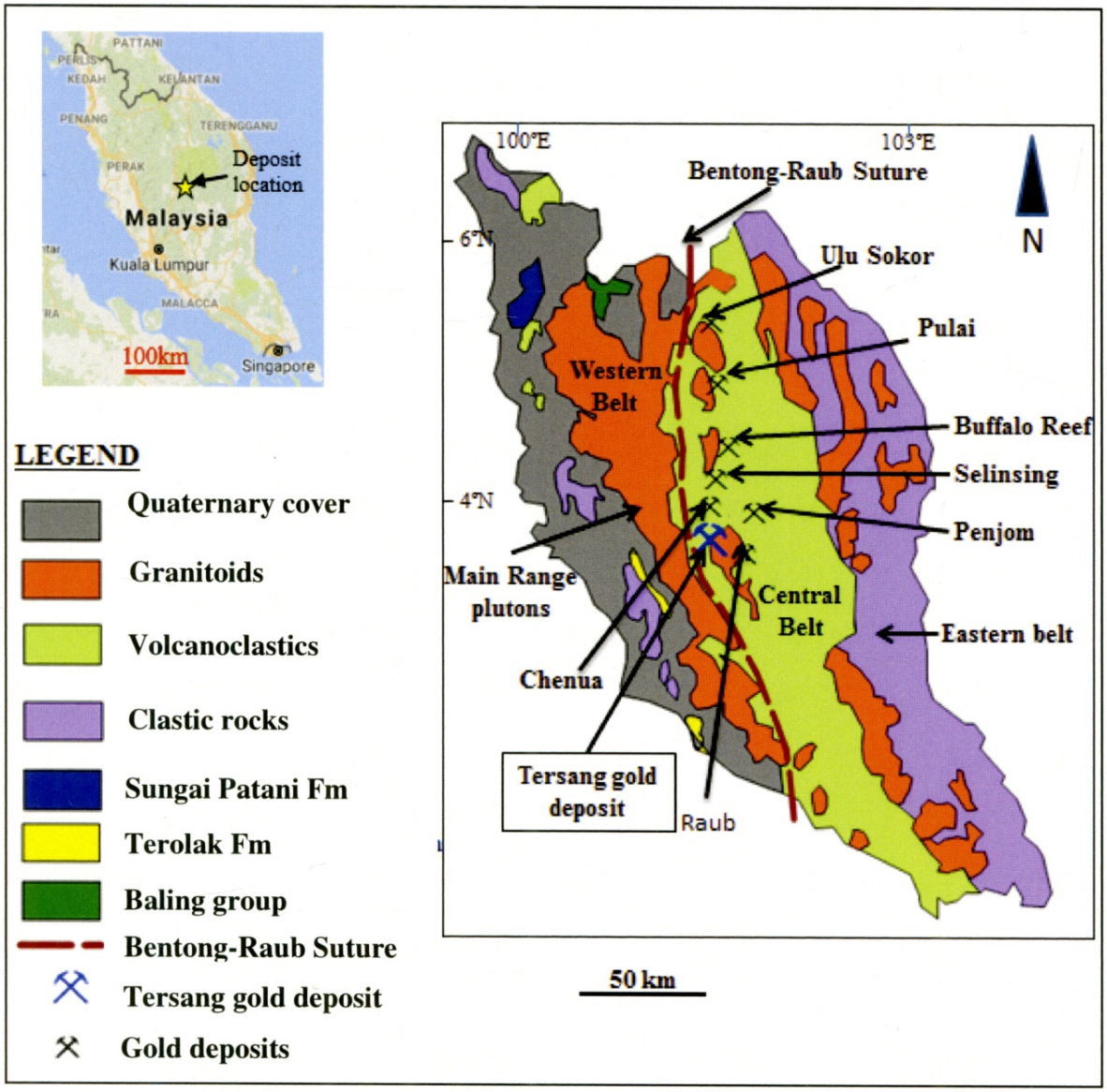

Figure 1. Map showing the location of the Tersang gold mine, the Bentong-Raub Suture Zone and the Western, Central, and Eastern Belts in Peninsular Malaysia.

The Bentong-Raub Suture Zone is a significant NW-SE trending fault system. The suture is suggested to be genetically related to the gold mineralisation in the mining district of the Central Gold Belt. The Bentong-Raub Suture Zone of the Malay Peninsula represents the main Palaeo-Tethys ocean basin and forms the boundary between the Sibumasu Terrane in the west and the Sukhothai Arc in the east [2]. The suture extends up to 20 km in width containing oceanic radiolarian cherts ranging in age from Devonian to Upper Permian [4]. Within this suture, there is mélange composed of clasts of ribbon-bedded chert, limestone, sandstone, conglomerate, turbidites, volcanic and volcaniclastic rocks. Additionally, bodies of serpentinite interpreted to be mafic/ultramafic rocks and oceanic peridotites are documented [17]. Chert and limestone clasts in the mélange were dated by radiolarians, conodonts and foraminifera and gave an age of Carboniferous and Permian [17]. Ages of metamorphism were determined from Schist and phyllite samples as being Ordovician, Silurian and Devonian. Consistently, the radiolarian cherts returned another wider age range from Devonian to Upper Permian [3].

3. Methods of Study

The methods of study described here include field work at the gold deposit area as well as laboratory work that were carried out at the ARC (Australian Research Council) Centre of Excellence in Ore Deposits (CODES), University of Tasmania, Australia. Field mapping was carried out recording lithology and structures at a scale of 1:2000. A GPS (global positioning system) was used to provide positions accurate to 3–10 m depending on the signal reception quality. In this study, coordinate systems are in UTM (Universal Transverse Mercator), zone 47, northern hemisphere (Map datum-WGS 84). If UTM and RSO (Rectified Skew Orthomorphic) systems were used, the coordinates were shown as northing and easting, typically in meters. At some locations, standard mine grids were converted to RSO or UTM for accurate locations of the mapped area. Thirty eight sedimentary rock and quartz vein samples were collected. List of samples is presented in Table 1.

The analytical techniques that were used in the study include: U-Pb zircon dating [18], Back-scattered imaging (BSE) and mineral spectra (EDS) using scanning electron microscope, Trace element determination in pyrite and mapping of pyrite grains by LA ICP-MS [19,20]. In addition, Cathodoluminescence (CL) imaging of zircon grains was carried out. These techniques are described below.

Table 1. List of samples collected in the field from the Tersang, mesothermal gold deposit, Malaysia.

Location	*Sample ID*	*X_UTM*	*Y_UTM*	*Z*	*Field Description*	*Visible mineral-alteration*	*Visible structure*
Main pit	TER-R001	812863	440915	148	Sandstone	Pyrite boxwork and FeO	Bedding and jointing
Main pit	TER-R002	812863	440917	154	Quartz vein		quartz vein intersection
Main pit	TER-R003	812863	440918	157	Quartz vein	Propylitic alteration	Bedding and jointing
Main pit	TER-R004	812863	440921	158	Quartz vein		Vein intersection
Main pit	TER-R005	812863	440926	161	Quartz vein	Disseminated Pyrite, FeO	quartz vein intersection
Main pit	TER-R006	812851	440918	164	Quartz vein	Disseminated Pyrite	Vein cuts bedding
Main pit	TER-R007	812851	440918	163	Sandstone	Disseminated Pyrite	Bedding
Main pit	TER-R008	812719	440890	142	Quartz vein		
Main pit	TER-R009	812719	440890	142	Quartz vein	Propylitic alteration	
Main pit	TER-R010	812719	440890	142	Quartz vein		
Main pit	TER-R011	812851	440920	151	Quartz vein	Disseminated Pyrite	Vein parallel to bedding
West of quarry	TER-R012	812846	440914	169	Quartz vein	Disseminated Pyrite	
West of quarry	TER-R013	812846	440911	171	Quartz vein	Disseminated Pyrite	Vein intersection
West of quarry	TER-R014	812861	440908	168	Quartz vein	Disseminated Pyrite	
Main pit	TER-R015	812858	440906	160	Quartz vein	Disseminated Pyrite	Vein intersection
Main pit	TER-R016	812836	440912	158	Quartz vein	Disseminated Pyrite	Quartz lens
Main pit	TER-R017	812791	440917	157	Quartz vein		Vein cuts across bedding
Main pit	TER-R018	812808	440883	158	Quartz vein		Vein parallel to bedding
Main pit	TER-R019	812808	440883	158	Quartz vein		Vein cuts across bedding
Main pit	TER-R020	812865	440891	170	Quartz vein		Vein intersection
Main pit	TER-R021	812871	440895	159	Quartz vein	Sulfide	
East of quarry	TER-R022	812889	440918	171	Quartz vein	Sulfide	Fault F1
East of quarry	TER-R023	812885	440927	178	Quartz vein	Disseminated Pyrite	Fault F1
East of quarry	TER-R024	812884	440931	179	Quartz vein	Propylitic alteration, sulfide	Fault F1
East of quarry	TER-R025	812881	440930	180	Quartz vein	Disseminated Pyrite	Vein parallel to Fault F1
East of quarry	TER-R026	812906	440994	175	Quartz vein	Disseminated Pyrite	
East of quarry	TER-R027	812894	440898	167	Quartz vein	Disseminated Pyrite	
Northwest	TER-R028	812630	441094	165	Rhyolite		
Northwest	TER-R029	812689	441071	174	Quartz vein	Disseminated Pyrite	Vein cuts across bedding
Northwest	TER-R030	812753	441009	182	Quartz vein	Disseminated Pyrite	Vein cuts across bedding
North	TER-R031	812723	441204	210	Quartz vein		
North	TER-R032	812782	441210	217	Fault breccia	Sulfide	
Northeast	TER-R033	812858	441160	226	Felsite		
East	TER-R034	812826	441070	221	Quartz vein	Sulfide	
East	TER-R035	812826	441120	226	Quartz vein	Sulfide	
Southeast	TER-R036	812910	440853	172	Quartz vein		
Southeast	TER-R037	812937	440938	204	Quartz vein		Vein parallel to fault plan
Southeast	TER-R038	812937	440938	204	Quartz vein		Vein parallel to fault plan
Southeast	TER-R039	812928	440904	186	Quartz vein	Sulfide	
Southeast	TER-R040	812920	440880	177	Quartz vein	Sulfide	
North	SM09-17A-B	812725	441170	211	Sandstone		
North	SM09-21	812783	441212	212	Rhyolite		

3.1. U-Pb zircon dating

Approximately 200 g of rock was crushed and milled in a Cr-steel ring mill to a grain size of less than 400 μm. Non-magnetic heavy minerals were then separated using a gold pan and a Fe-B-Nd hand magnet. The zircons were hand-picked from the heavy mineral concentrate under the microscope in cross-polarised transmitted light. The standard procedure for the LA ICP-MS zircon dating is performed on an Agilent 7500cs quadrupole ICPMS with a 193 nm coherent Ar-F gas laser and the resonetics M50 ablation cell.

The downhole fractionation, instrument drift and mass bias correction factors for Pb/U ratios on zircons were calculated using two analyses on the primary (91500 standard of Wiendenbeck [21]) and one analysis on each of the secondary standard zircons [22,23] analysed at the beginning of the session and every 12 unknown zircons (roughly every 1/2 hour) using the same spot size and conditions as used on the samples. Additional secondary standards (The Mud Tank Zircon of Black and Gulson [24] were also analysed. The correction factor for the 207Pb/206Pb ratio was calculated using three large spots of NIST610 analysed at the beginning and the end of the day and corrected using the values recommended by Baker [25]. Each analysis on the zircons began with a 30 second blank gas measurement followed by a further 30 seconds of analysis time when the laser was switched on. Zircons were sampled on 32 micron spots using the laser at 5 Hz and a density of approximately 1.5 J/cm2. A flow of He carrier gas at a rate of 0.6 liters/minute carried particles ablated by the laser out of the chamber to be mixed with Ar gas and carried to the plasma torch.

Isotopes measured include 49Ti, 96Zr, 146Nd, 178Hf, 202Hg, 204Pb, 206Pb, 207Pb, 208Pb, 232Th and 238U with each element being measured sequentially every 0.16 s with longer counting time on the Pb isotopes compared to the other elements. The data reduction used was based on the method outlined in detail in Meffre [26] similar to that outlined in Black [25] and Paton [27]. Element abundances on zircons were calculated using the method outlined by Kosler [18] using Zr as the internal standard element, assuming stoichiometric proportions and using the 91500 to standard correct for mass bias.

3.2. LA-ICP-MS analysis technique

Trace element analysis and imaging of pyrite were undertaken using the LA-ICP-MS facility at CODES, University of Tasmania. Analyses were done using a Newwave UP213 laser ablation microprobe coupled with an Agilent 7500 or 7700 ICP-MS. Samples were ablated in He and mixed with Ar before reaching the ICP-MS. Calibration was carried out with the in-house standard (STDGL2b2), which is a lithium borate fused glass disk, with known concentrations of trace elements [19]. The standard was analysed at regular intervals during analysis to correct for drift and mass bias. For standard set-up, the Fe concentration was tabulated at 465000 ppm (46.5 %) for pyrite. To minimize surface contamination, sulphides were pre-ablated with laser

pulses. For pyrite imaging, the laser was rastered across the sample in a series of parallel lines. The spot size of the laser was 22μm during pyrite mapping and there was no space between the lines. All the data was binned to give the pixels in the maps.

Each line was pre-ablated before analysis. The backgrounds were recorded before each image and subtracted from each analysis line [18]. A total of twenty-nine elements were analysed by LA-ICP-MS from pyrites including: Na, Mg, Al, Si, K, Ca, Ti, V, Cr, Mn, Fe, Co, Ni, Cu, Zn, As, Se, Mo, Ag, Sb, Te, W, Pt, Au, Hg, Tl, Pb, Bi and U. The element maps were processed as follows: First, the trace element maps were converted from count per second into part per millions (ppm) in order to get a robust representation of element concentration for each pyrite type. Secondly, the csv files were imported into ioGAS© which is an advanced geochemical exploratory data analysis software package. Thirdly, pyrite phases were recognized based on element distribution on each pyrite map. In total, four pyrite phases were identified using ioGAS© software in terms of high content in Te, As and low content in Au and As. In ioGAS software, a clustering method was used by uploading all pyrite pixel data in the form of csv data. Furthermore, an attribute map was made on which pyrite boundaries of all analyzed grains were displayed. Each pyrite phase was discriminated digitally and assigned a colour. In addition, each pyrite phase outline or boundary that is shown on LA-ICPMS maps has been drawn by hands (Figures 2–8).

Finally, pyrite phase values were calculated by grouping all the pixels belonging to a given pyrite phase. Other datasets such as minimum, maximum, median, and standard deviation for the pyrite phases 1, 2, 3, and 4 are also documented. Additionally, the Pearson coefficients of correlation among Au and other trace elements for pyrite phases 1, 2, 3, and 4 are presented in Tables 8A–D. Positive correlation implies that both variables tend to move in the same direction: If one variable increases, the other tends to also increase. If one decreases, the other tends to also. Negative correlation means that the variables tend to move in the opposite directions: If one variable increases, the other tends to decrease, and vice-versa. Correlation matrix was calculated for each pyrite phase by looking at the relationship among Au and other trace elements. In this paper, we use a weak correlation for the coefficients that vary from 0.3 to 0.4. A moderate correlation is considered for coefficients ranging from 0.5 to 0.6 and a strong correlation for numbers above or equal to 0.7 [28].

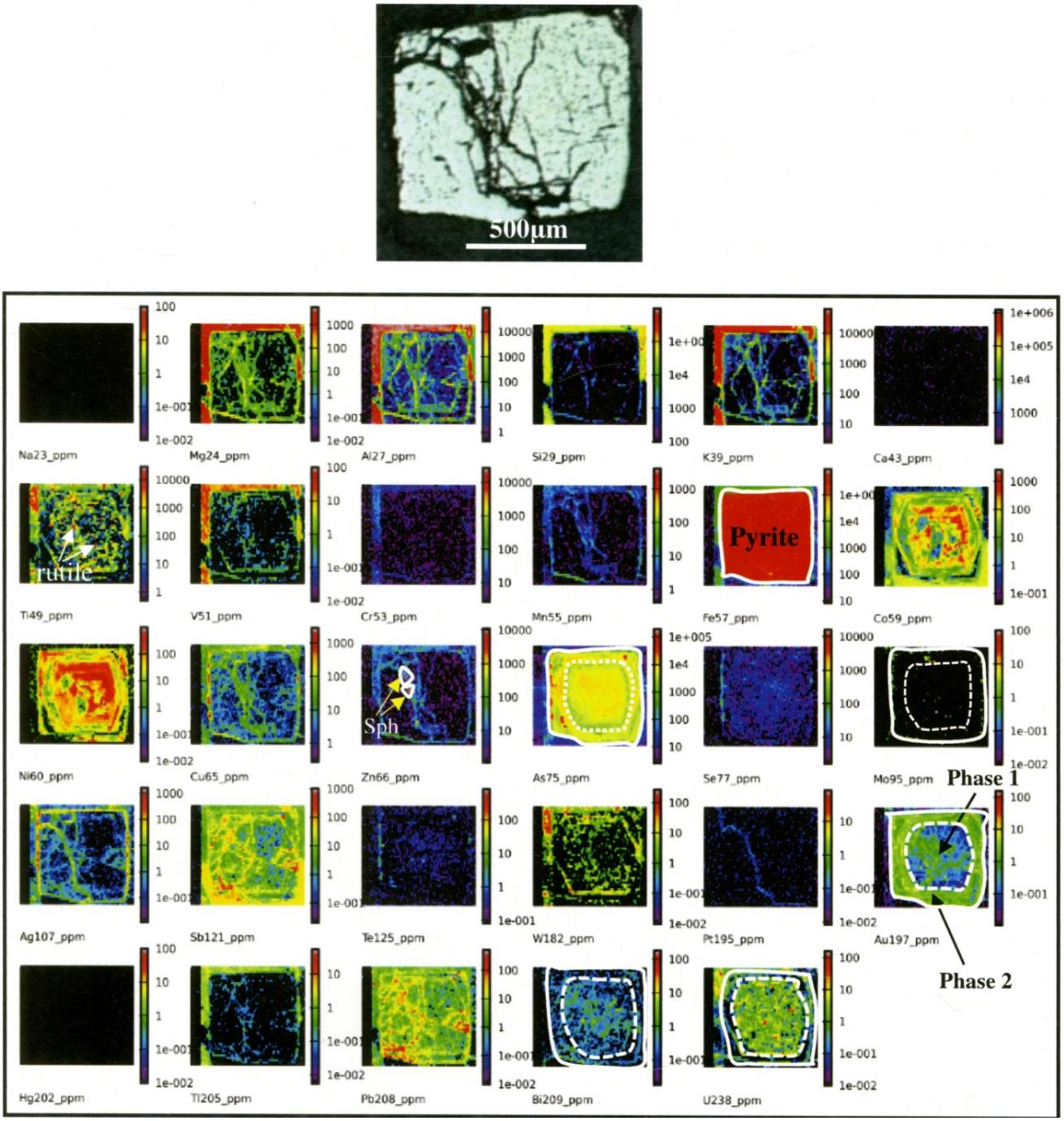

Figure 2. LA-ICPMS pyrite map of euhedral pyrite contained in the host sandstone. This map shows silicates concentrated mostly in matrix and some are found in internal fractures. Elements such as Ni and Co display zoned patterns as well as Au. Gold concentrations are commonly present in the core (pyrite phase 1) and margin of pyrite (pyrite phase 2). Inclusions rich in Sb-Pb, W, As and U are presents. Additionally, rutile and sphalerite inclusions are mapped out. Chalcopyrite inclusions are preferentially present in the rim of pyrite phase 2. Elevated Au concentrations are shown in the inner zone (core) and outer zone (margin/rim).

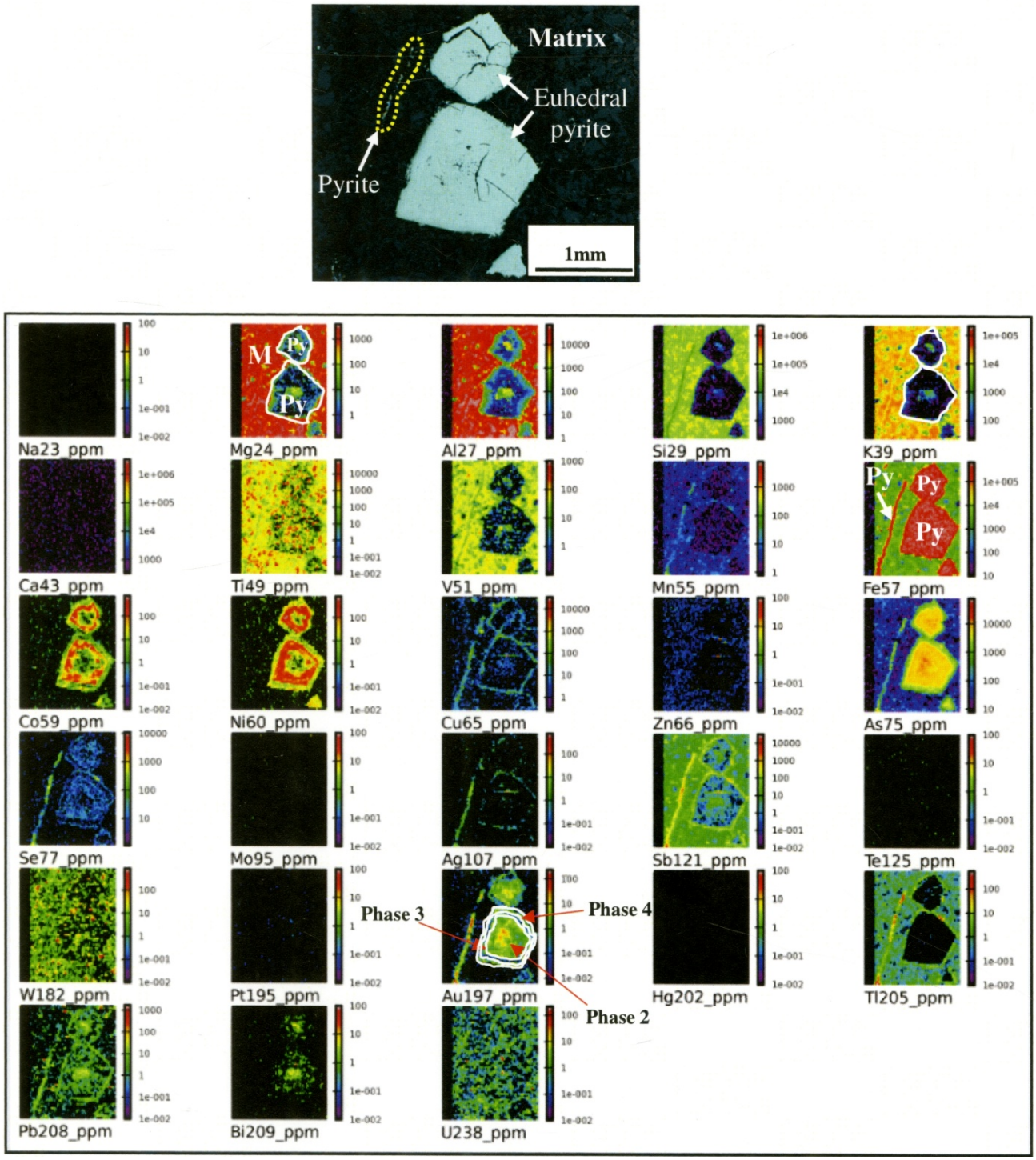

Figure 3. LA-ICPMS pyrite map showing pyrite phases 2, 3, and 4 from the host sandstone. Silicates are present in the matrix. Inclusions enriched in Au-Tl-Sb are common in the aggregates. W-rich inclusions are sparse in the pyrite lattice as well as Ti-rich (rutile) inclusions. Gold content (>1 ppm Au) is elevated in pyrite phase 2. Low levels of silicates (Mg-Al-K rich) are also recorded in pyrite phase 2.

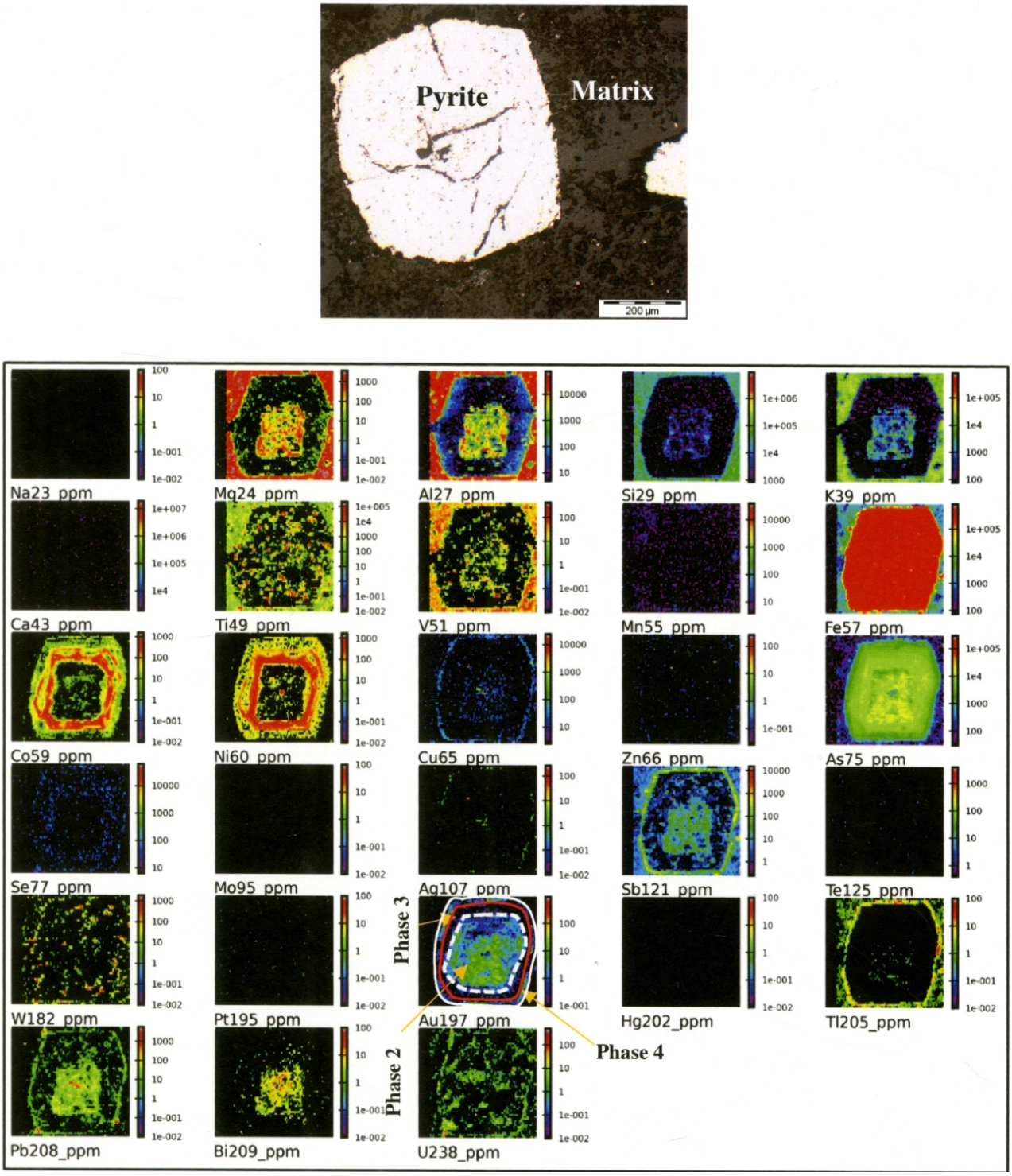

Figure 4. LA-ICPMS pyrite map showing pyrite phases 2, 3, and 4. Phase 2 is characterized by elevated Au, Pb, Bi, Sb and As contents. Phase 3 has elevated Co and Ni concentration and phase 4 has elevated Tl, Pb, Sb contents. Ti-rich (rutile) inclusions are numerous in the Titanium pixel image. Few inclusions of Pb-rich (galena) are spotted in the core and rim of pyrite. Pyrite rims are enriched in Pb, Sb and Tl.

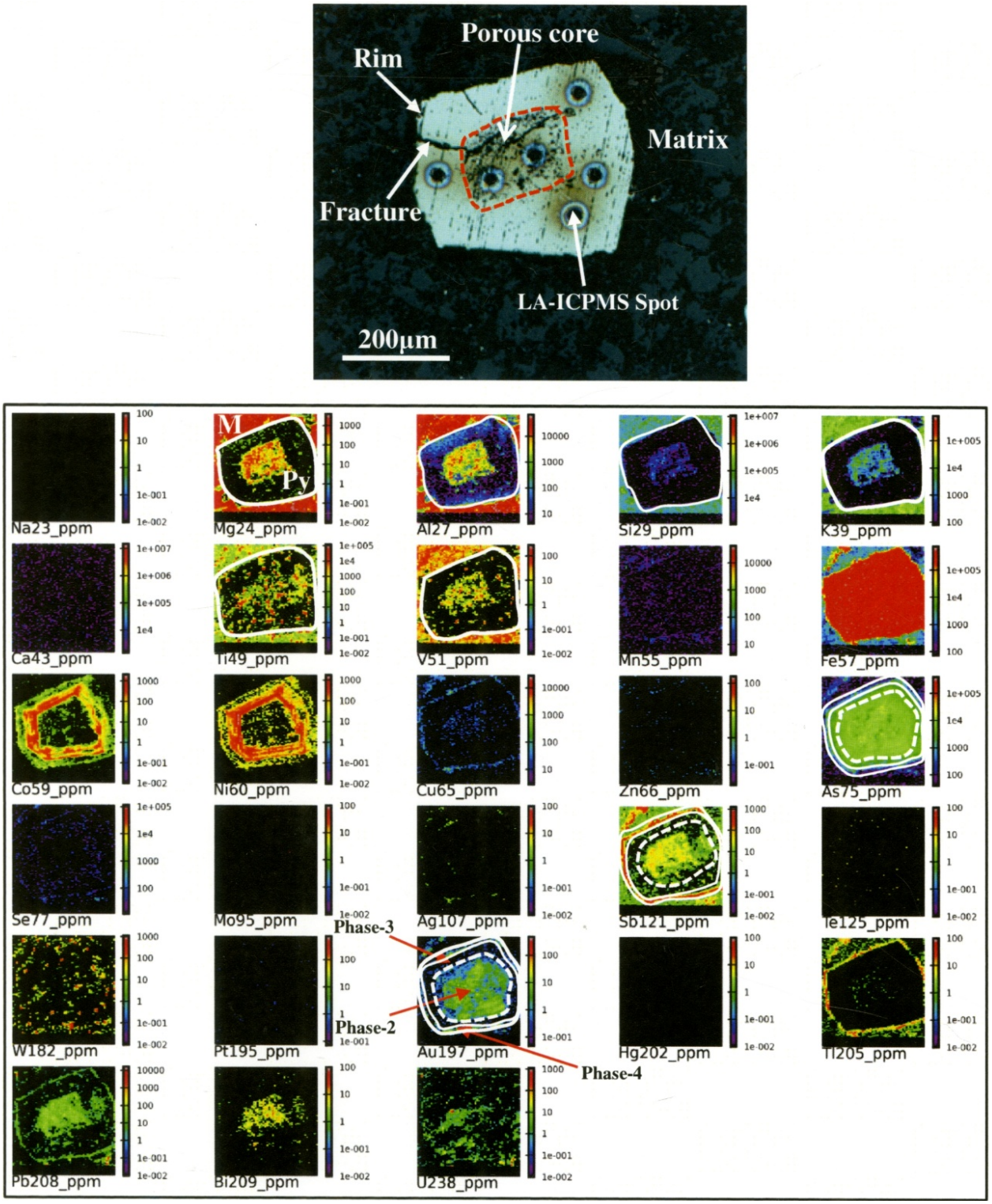

Figure 5. LA-ICPMS images of pyrite showing three pyrite phases: phase 2 has elevated Au, Pb, Bi, Sb, and As contents; phase 3 has elevated Ni and Co, low level of As and phase 3 consists of Minor concentration of Ni, Co, Pb, As combined elevated content of Tl along in the rim. Phase 2 has the highest Au concentration compared to phases 3 and 4.

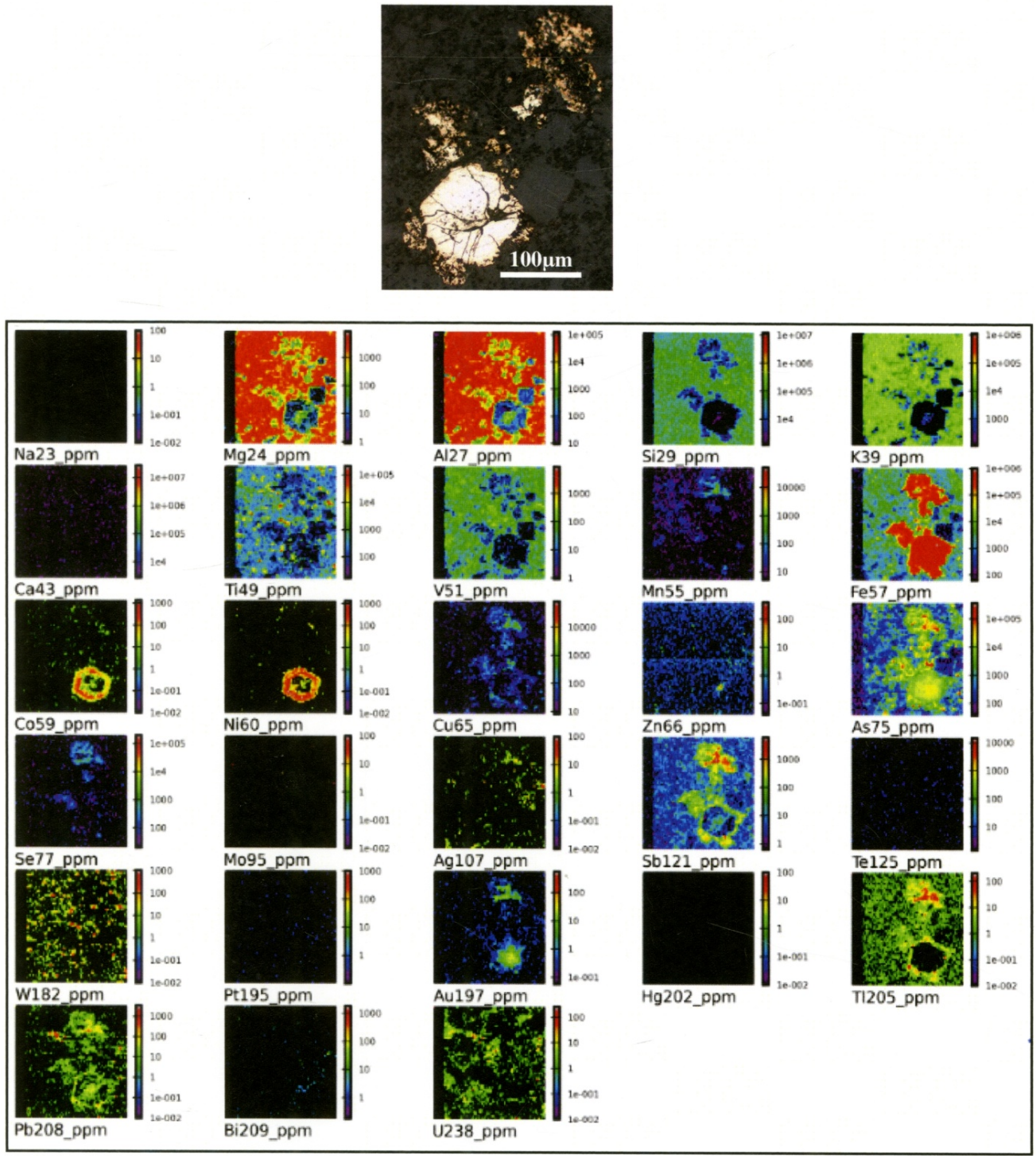

Figure 6. LA-ICPMS images of pyrite aggregates indicating the presence of inclusions of arsenopyrite, rutile, as well as W-, Pb-, and U-rich inclusions. The pyrite aggregates are characterized by elevated levels of As, Sb, Tl, Co, and Ni and low levels of Au, Pb, U and W. In addition, traces of Cu, Zn and Se. Matrix (zoned located outside of the pyrite lattice) has elevated contents of chemical elements such as Mg and Al, which are part of aluminosilicate composition commonly found in sandstone.

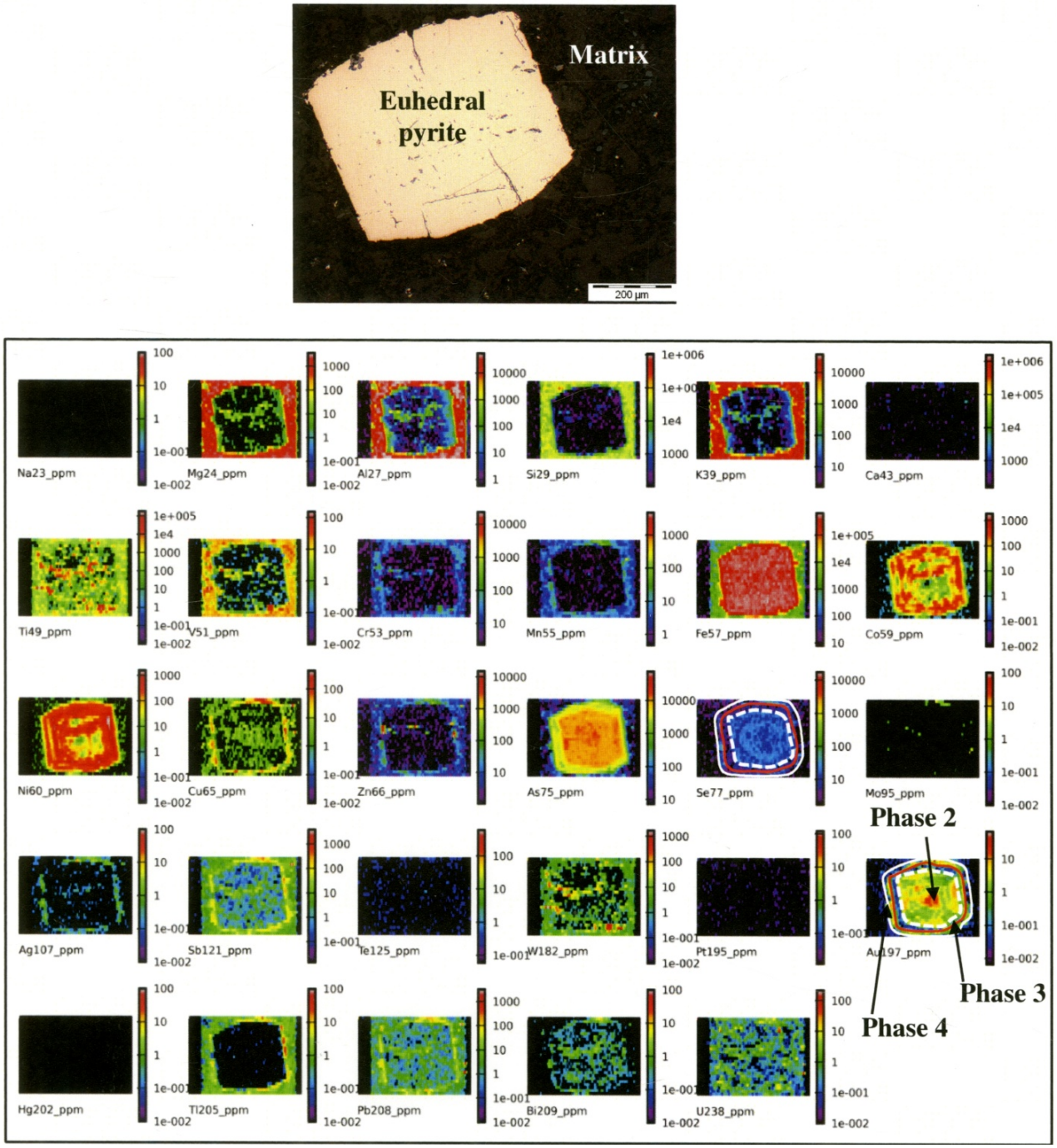

Figure 7. LA ICP-MS images of trace elements in pyrite showing three phases of pyrite namely phases 2, 3, and 4. The Ti image shows rutile inclusions. Phase 2 shows elevated levels of As, Co, Ni and Au. Phase 3 has elevated Co and Ni. Phase 4 is particularly enriched Cu, Sb, Tl, Pb, Bi, and Ag. The Zn image shows few sphalerite inclusions. The presence of W-U rich inclusions are common.

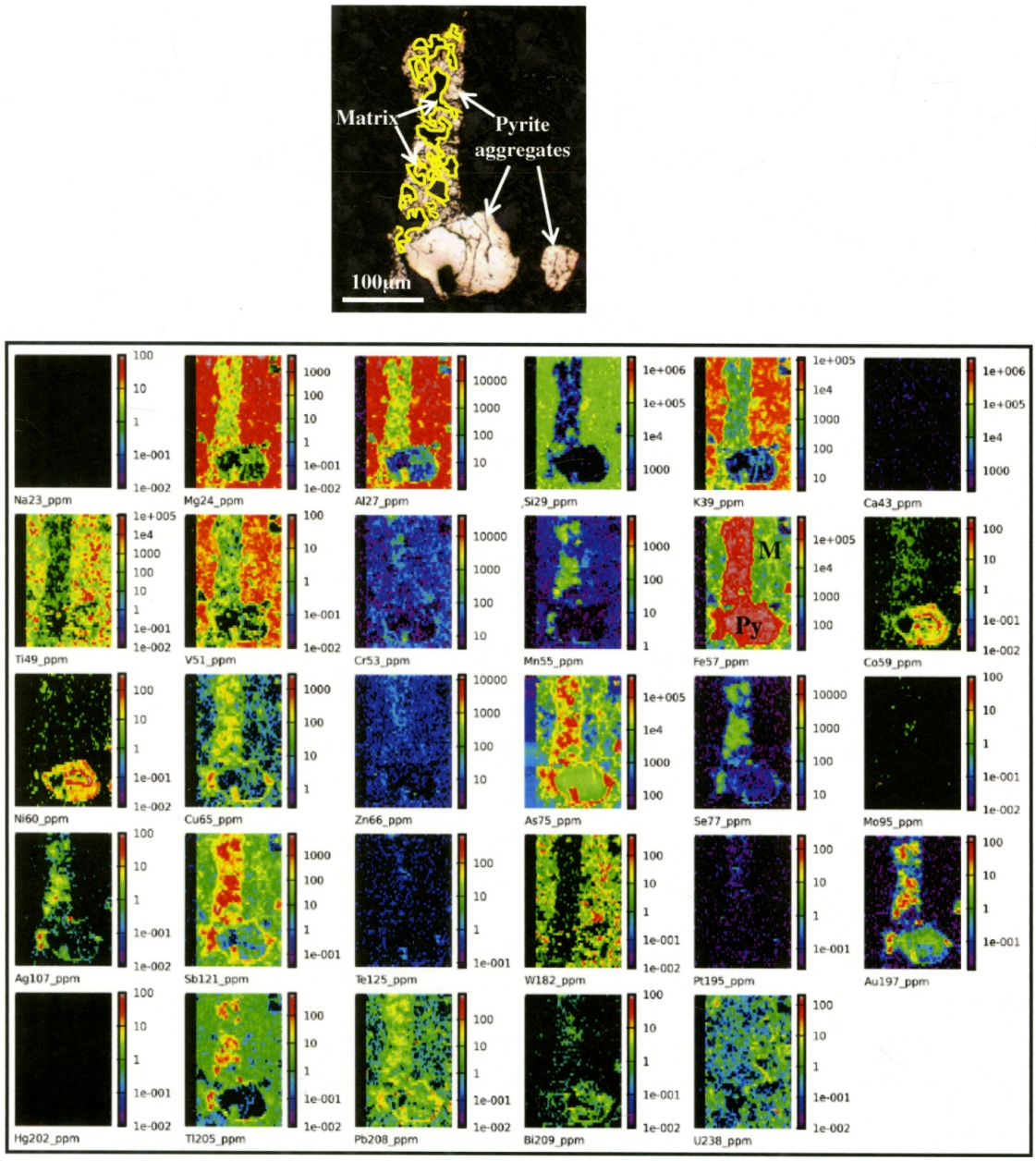

Figure 8. LA-ICPMS images of trace elements showing rutile inclusions in the matrix with elevated vanadium concentration. The pyrite aggregates recorded a complex mix of pyrite phases. Trace elements such as Cu, As, Sb, Au, Tl and Pb have elevated contents in the pyrite aggregates. Low concentrations of Se and Ag are present.

4. Local and Deposit Geology

4.1. Local geology

Haile [29] documented that the Tersang gold deposit lies within a Carboniferous sequence, which comprises shale, quartzite, conglomerate, phyllite belonging to the Raub Formation or

Group. These authors correlated the Tersang sedimentary and metamorphic rocks to those of the Raub Group based on lithological features. In addition, these rocks are overlain by Carboniferous to Permian calcareous shale. In the northwest of the Tersang area, tuff sequences overlie the calcareous shale and contain fossils, indicating an age range from Carboniferous to Triassic. In the north (Figure 9), occurrences of felsic igneous rocks may be the extension of the rhyolite that crops out in the open pit. The local geology map (Figure 9) also displays the locality of the Selinsing gold deposit further north. To the west, gabbroic bodies are common and associated with the Bentong-Raub Suture rocks. To the east, intermediate igneous rocks crop out.

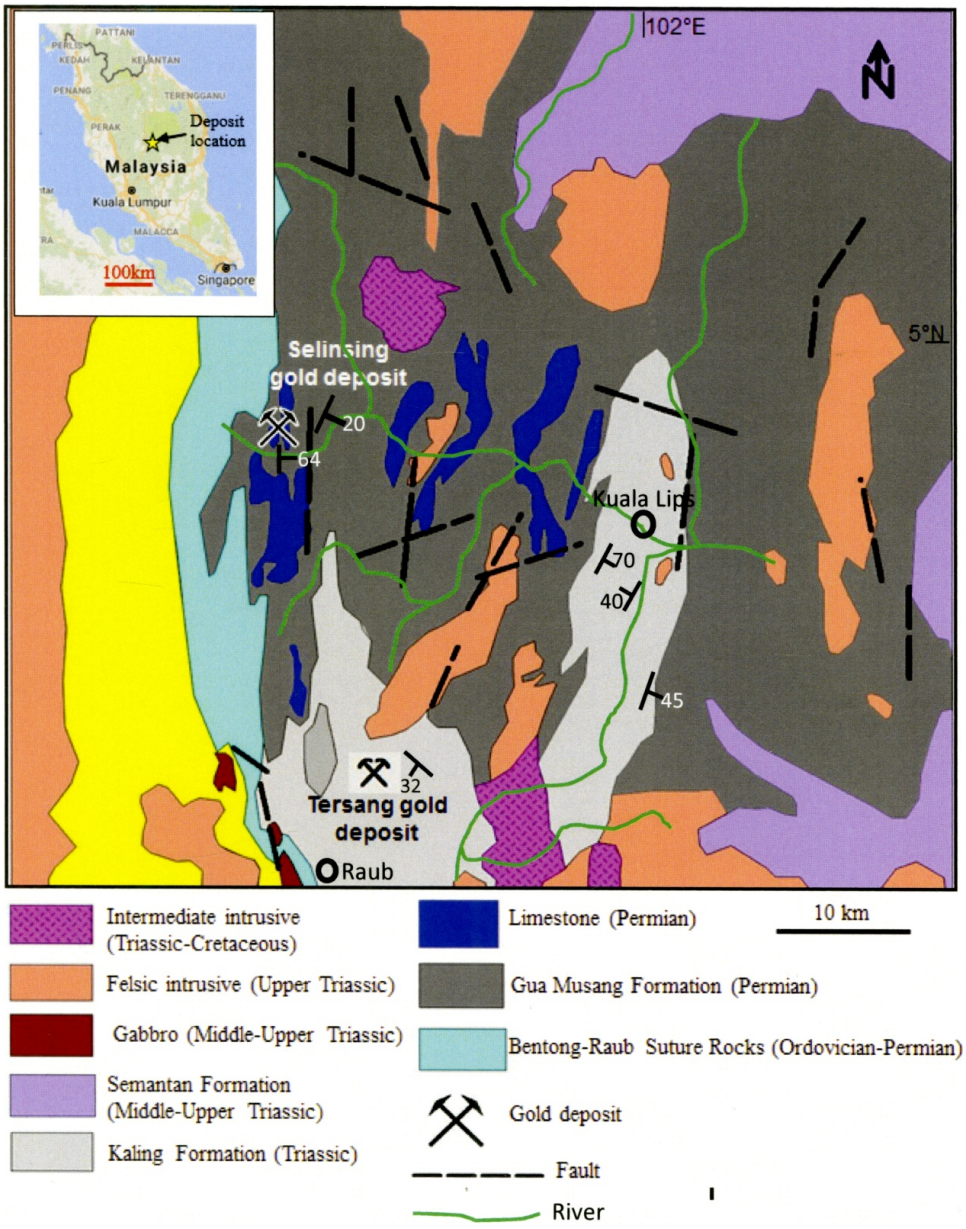

Figure 9. Map of local geology showing localities of the Tersang and Selinsing gold deposits in the Central Gold Belt, Peninsular Malaysia.

4.2. Deposit geology

The Tersang gold deposit is characterised by a belt of gold mineralisation trending NS and comprises 1800 m long rhyolite body mixed up with shale and sandstone (Figure 10). The ore zone is characterised by the presence of sheeted quartz veins and sulphide mineralisation hosted in the sandstone and rhyolite. In the north, the rhyolite occurs associated with siltstone and shale beds and also overprinted quartz stockwork. Tuff sequences crop out in the northwest, underlying the shale strata. In the south of the mineralised corridor, the main lithologies are made up of sandstone, breccia and rhyolite in a highly tectonized area. This zone contains multitude of quartz stockwork veins (Figure 10). The area that was mapped during this study is situated between northing 812600 m and 81300 mN and easting 440800 m and 441300 mE (UTM system) (Figure 10). The area represents the open pit, comprising grey sandstone and breccia, which are interfingered with rhyolite. The white area on the mine-scale map (Figure 10) represents the Kaling Formation shown in grey colour on the district-scale map in Figure 9.

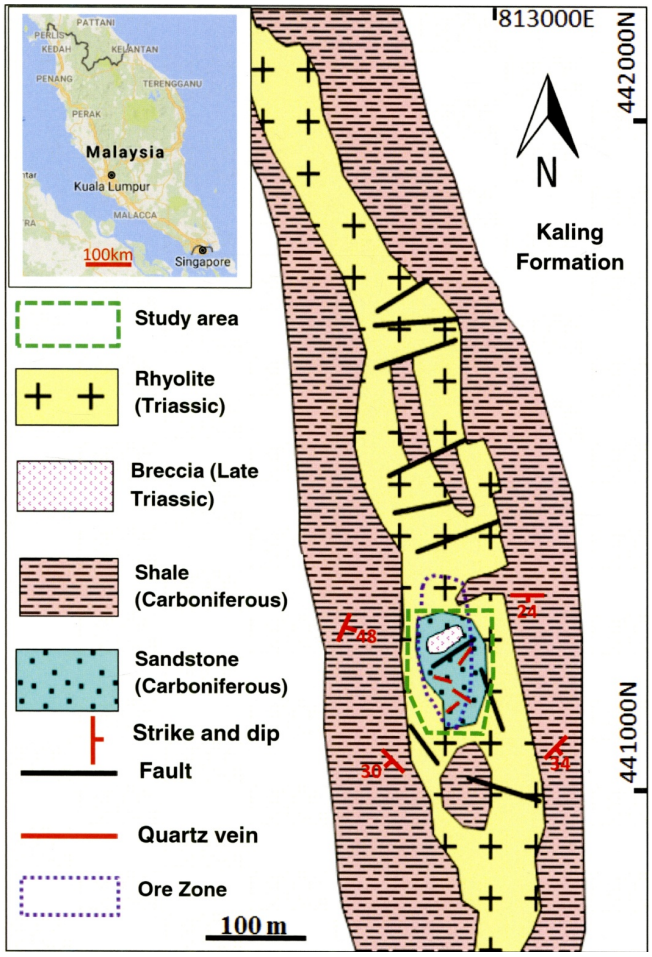

Figure 10. Deposit-scale geology at the Tersang gold deposit showing the belt of mineralisation (Modified from Makoundi, 2012).

The Tersang northern zone was not considered in this study as it is forested with lack of fresh outcrops. The sandstones are commonly eroded locally in the mining area and the geologic contact between the sandstones and shales (partly metamorphosed to phyllite) is hardly visible. The sandstone crops out in the open pit (the central part) and the southern part of the deposit (Figure 11a), and is grey in colour when less weathered. The sandstone is fine-grained, poorly sorted in contact with the chilled margins in the northwest and northeast parts of the deposit (Figure 11b).

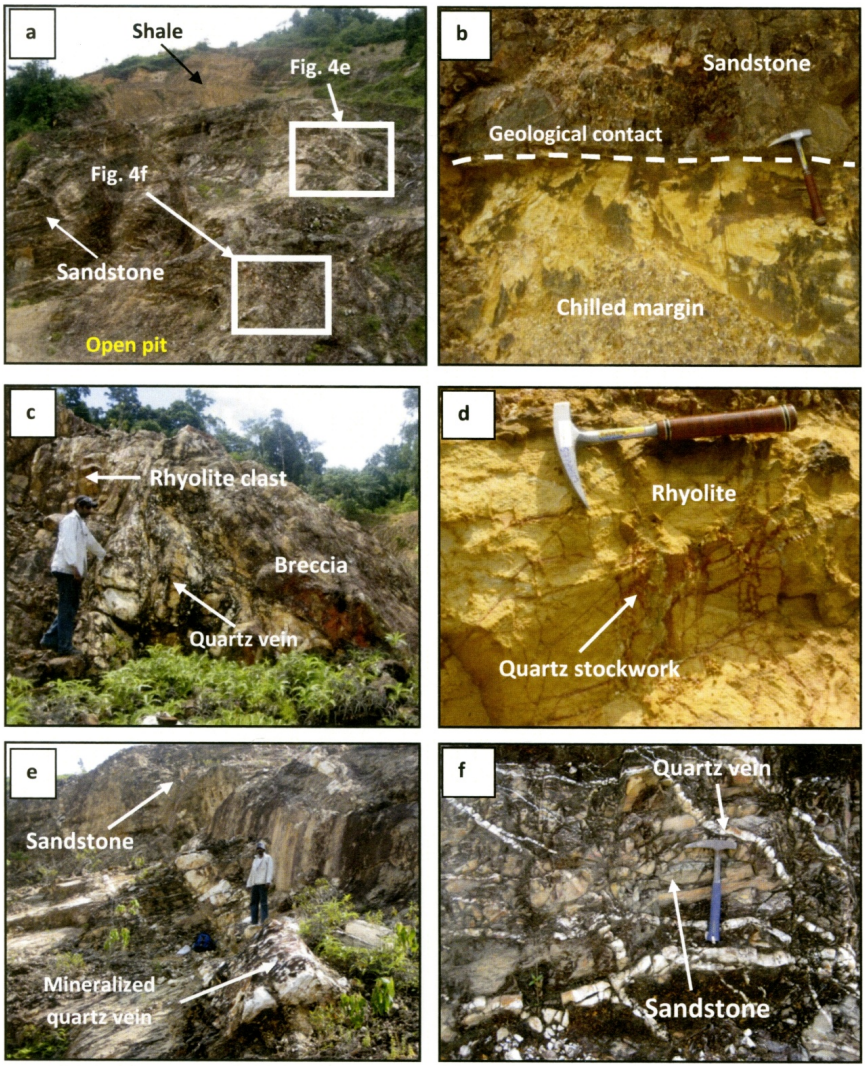

Figure 11. Outcrop photographs at the Tersang gold deposit. (a) Open pit image looking north. (b) Geological contact between sandstone and rhyolite. (c) Breccia exposure. (d) Rhyolite and quartz stockwork. (e) Mineralised quartz vein (stage 1). (f) Quartz stockwork in the sandstone.

The sandstone contains pyrite grains and veins and its petrography consists of quartz (60 vol. %), K-feldspar (10 vol. %), biotite (20 vol. %), and disseminated pyrite (up to 10 vol. %). A greyish brown, oxidised breccia unit of 40–50 m in length and 20–25 m in width crops out within the rhyolite unit (Figure 11c). The breccia, under the microscope shows rhyolite and sandstone angular fragments

(60 vol. %) and matrix (40 vol. %). The fragments have a size ranging from 0.3 to 1 cm. Small-scale stockworks of quartz veinlets (up to 200 μm thick) are also present. Oxidised pyrite grains are contained in some rock fragments. The matrix is mainly siliceous and contains iron oxides.

The rhyolite associated with quartz stockwork is exposed over an area of approximately 600 m long and 400 m wide in the central and northern parts of the deposit (Figure 11d). Thin section studies revealed the presence of quartz (70 vol. %), K-feldspar (10 vol. %), muscovite (10 vol. %), and pyrite (up to 10 vol. %). In addition, muscovite occurs in the form of laths and interstitial infillings. Two stages of mineralised quartz veins were delineated: Stage 1 vein trends NNW-SSE (Figure 11e) and stage 2 vein strikes ESE-WNW (Figure 11f). Lithological and mineralogical characteristics of host rock and intrusion are shown in Figure 12. The list of samples and their descriptions is documented in Table 1.

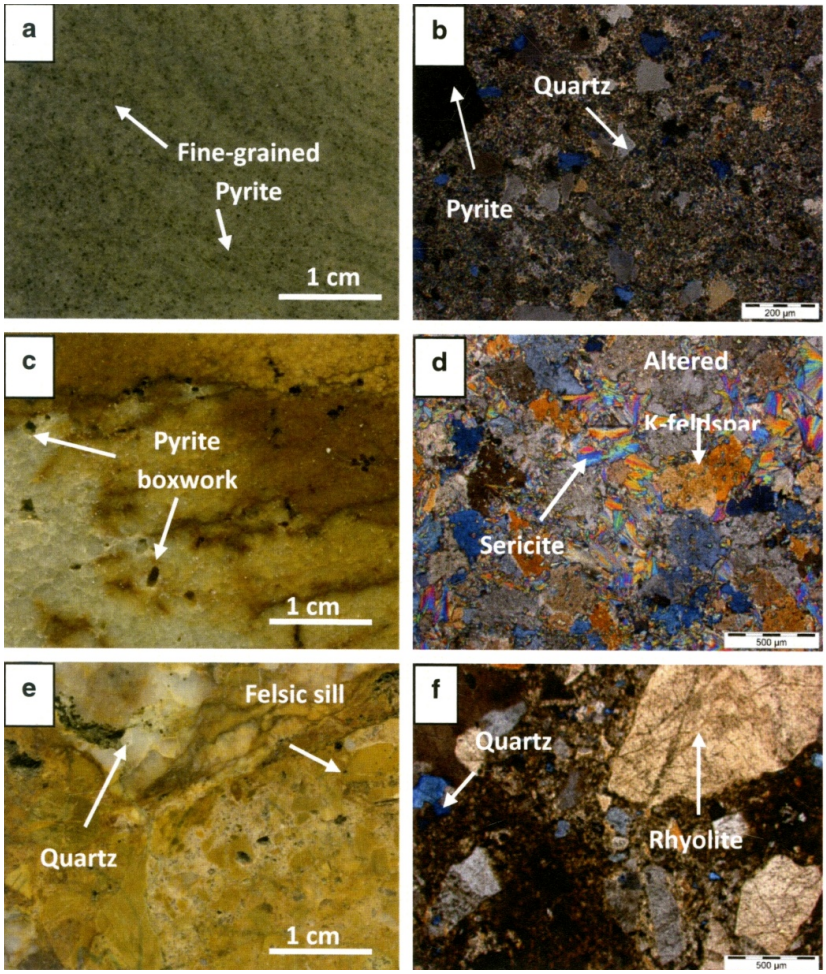

Figure 12. Lithological characteristics of host rocks and intrusion at the Tersang gold deposit. (a) Photograph of Host sandstone (sample TER-R007). (b) Photomicrograph of Host sandstone (sample TER-R007). (c) Felsic intrusion (sample TER-R033). (d) Photomicrograph of the intrusion (sample TER-R033). (e) Photograph of breccia (sample TER-R032). (f) Photomicrograph of the breccia.

5. U-Pb Zircon Dating

The host sandstone and rhyolite were sampled and analysed for age determination. Results of the U-Pb zircon geochronology are shown in Tables 2–5. The calculation of ages is on 1σ error on each concordia plot. A hand specimen of sandstone (sample SM09-17a) was analysed (Figure 13a). The seven youngest zircons have a mean age of 333.5 ± 2.5 Ma (MSWD = 1.2) and a median value of 333 Ma indicating an Early Carboniferous age (Mississippian). The detrital zircon populations are at ca. 250–400 Ma, ca. 875 Ma and ca.1100 Ma. Th/U values range from 0.07 to 1.56. CL imaging shows that the detrital zircon grains are sub-angular with oscillatory zoning. Results of the U-Pb zircon dating of this sample are presented in Table 2.

From the upper part of the stratigraphy, a sandstone specimen (sample SM09-17b) was collected and analysed (Figure 13b). Five youngest detrital zircons returned a mean maximum depositional age of 261.5 ± 4.9 Ma at 95% confidence with MSWD = 1.3. The median age is 265 Ma indicating an Early Permian maximum depositional age. The detrital zircon population peaks are at ca. 200–510 Ma, ca. 750 Ma; ca. 1340 Ma, ca. 1560–2030 Ma, ca. 2760 Ma. The Th/U values are greater than 0.1 apart from a single value of 0.1 corresponding to a zircon grain that suffered Pb loss. CL images of the zircon show elongated zircon grains having concealed or not well developed oscillatory zoning. The only Th/U ratio < 0.1 corresponds to the mixing age domain of the analysed zircon grain. Results of the U-Pb zircon dating of this sample are presented in Table 3.

A sandstone specimen (sample TER-R007), collected from the lowest part of the stratigraphy was analysed (Figure 13c). The four youngest zircon grains have a mean maximum depositional age of 319.3 ± 5.3 Ma (MSWD = 0.63) and the median age is 320 Ma indicating an Early Carboniferous (Mississippian). The sample yields detrital zircon population peaks at ca. 300–500 Ma and ca. 1400–1600 Ma. The Th/U ratio values are all above 0.1 strongly indicating typical igneous origin of the zircons. The zircon grains show thinly developed oscillatory zoning and the grains are angular to sub-angular with some fragmented edges (Figure 13 and Figure 14). Results of the U-Pb zircon dating of this sample are presented in Table 4.

A rhyolite (sample SM09-21) was analysed (Figure 13d) and the age of the 12 analyses ranges from 207 to 231 Ma. The age of 207 Ma was removed from the main population as it may have suffered post-crystallization Pb loss. The Pb loss is likely related to circulation of metamorphic fluids evidenced by the presence of CO_2-rich fluids in quartz veins. Post-crystallization Pb loss can lead to new zircon nucleating on previous undissolved crystals.

The remaining 11 analyses range from ca. 215 Ma to ca. 231 Ma (median ca. 222 Ma). The age of the rhyolite is evaluated at 218.8 ± 1.7 Ma (MSWD = 1.2) (Late Triassic) based on the six youngest zircon but the remaining may represent an inherited component of the rhyolite. The Th/U ratio values are all above 0.1. Overall, 98% of analysed zircons have Th/U values greater than 0.1 and only 2% are below 0.1. The Th/U ratio shows values greater than 0.1 typical for igneous zircons [30,31]. CL images show euhedral zircon grains with well-developed oscillatory zoning. Results of the U-Pb zircon dating of this sample are presented in Table 5.

Table 2. Results of U-Pb zircon dating of the host sandstone (sample SM09-17a).

	207 cor 206Pb/238U	*+/-1 ster*	*206Pb/238U*	*+/-1 RSE*	*207Pb/206Pb*	*+/-1 RSE*	*238U/206Pb*	*+/-1 std err*	*207Pb/206Pb*	*+/-1 std err*	*206Pb/238U*	*+/-1 ster*
SM09-17a			0.0136	1.5%	0.0479	6.3%	73.42	1.10	0.0479	0.0030	87	149
SM09-17a	303	3	0.0497	1.1%	0.0795	4.8%	20.10	0.22	0.0795	0.0039	313	96
SM09-17a	314	9	0.0521	2.8%	0.0862	25.3%	19.18	0.54	0.0862	0.0218	328	489
SM09-17a	331	3	0.0532	1.0%	0.0606	2.1%	18.79	0.18	0.0606	0.0013	334	45
SM09-17a	333	3	0.0530	0.9%	0.0535	3.3%	18.86	0.17	0.0535	0.0017	333	74
SM09-17a	335	2	0.0535	0.7%	0.0564	2.2%	18.69	0.13	0.0564	0.0013	336	49
SM09-17a	335	2	0.0535	0.7%	0.0566	2.2%	18.68	0.13	0.0566	0.0012	336	48
SM09-17a	337	7	0.0541	2.0%	0.0586	4.5%	18.50	0.37	0.0586	0.0027	339	99
SM09-17a	361	4	0.0588	1.1%	0.0691	3.9%	17.01	0.19	0.0691	0.0027	368	81
SM09-17a	368	3	0.0589	0.8%	0.0549	2.5%	16.99	0.14	0.0549	0.0014	369	56
SM09-17a	371	3	0.0593	0.7%	0.0542	1.9%	16.87	0.12	0.0542	0.0010	371	42
SM09-17a	434	3	0.0699	0.6%	0.0577	1.9%	14.31	0.09	0.0577	0.0011	435	41
SM09-17a	435	4	0.0701	1.0%	0.0580	3.2%	14.27	0.14	0.0580	0.0018	437	69
SM09-17a	436	4	0.0704	1.1%	0.0609	3.1%	14.19	0.15	0.0609	0.0019	439	68
SM09-17a	442	3	0.0712	0.6%	0.0575	2.0%	14.05	0.09	0.0575	0.0011	443	44
SM09-17a	446	2	0.0717	0.5%	0.0559	1.2%	13.95	0.08	0.0559	0.0007	446	26
SM09-17a	450	4	0.0723	0.8%	0.0558	2.1%	13.84	0.11	0.0558	0.0012	450	46
SM09-17a	471	4	0.0758	0.9%	0.0563	3.3%	13.20	0.12	0.0563	0.0019	471	73
SM09-17a	473	3	0.0764	0.6%	0.0588	1.7%	13.10	0.08	0.0588	0.0010	474	38
SM09-17a	495	10	0.0814	2.0%	0.0726	4.0%	12.29	0.25	0.0726	0.0029	504	82
SM09-17a	606	102	0.1022	17.0%	0.0890	16.3%	9.79	1.67	0.0890	0.0145	627	312
SM09-17a	887	7	0.1522	0.9%	0.0943	2.6%	6.57	0.06	0.0943	0.0024	913	49
SM09-17a	1146	6	0.1977	0.6%	0.0910	1.0%	5.06	0.03	0.0910	0.0009	1163	19

Table 3. Results of U-Pb zircon dating of the host sandstone (sample SM09-17b).

	207 cor 206Pb/238U	*+/-1 ster*	*206Pb/238U*	*+/-1 RSE*	*207Pb/206Pb*	*+/-1 RSE*	*238U/206Pb*	*+/-1 std err*	*207Pb/206Pb*	*+/-1 std err*	*206Pb/238U*	*+/-1 ster*
SM09-17b	260.25	5	0.04	0.02	0.06	0.03	23.92	0.43	0.06	0.00	294.18	7.80
SM09-17b	265.46	4	0.04	0.01	0.06	0.03	23.42	0.33	0.06	0.00	318.65	5.66
SM09-17b	266.32	6	0.04	0.02	0.09	0.05	22.71	0.50	0.09	0.00	386.46	11.23
SM09-17b	323.42	3	0.05	0.01	0.07	0.01	18.98	0.16	0.07	0.00	394.41	7.32
SM09-17b	337.42	3	0.05	0.01	0.06	0.02	18.49	0.18	0.06	0.00	370.44	5.87
SM09-17b	338.65	4	0.05	0.01	0.06	0.02	18.36	0.20	0.06	0.00	385.33	7.32
SM09-17b	352.52	8	0.06	0.02	0.08	0.05	17.14	0.37	0.08	0.00	499.45	20.30
SM09-17b	360.60	3	0.06	0.01	0.06	0.01	17.27	0.16	0.06	0.00	324.65	5.20
SM09-17b	362.04	4	0.06	0.01	0.06	0.02	17.25	0.19	0.06	0.00	360.74	5.55
SM09-17b	368.59	4	0.06	0.01	0.06	0.02	16.82	0.18	0.06	0.00	425.79	7.34
SM09-17b	403.98	3	0.06	0.01	0.06	0.01	15.39	0.13	0.06	0.00	377.22	5.33
SM09-17b	404.48	5	0.07	0.01	0.07	0.02	15.21	0.19	0.07	0.00	453.77	10.83
SM09-17b	435.12	4	0.07	0.01	0.07	0.01	14.08	0.12	0.07	0.00	498.65	6.54
SM09-17b	475.98	5	0.08	0.01	0.06	0.02	12.99	0.14	0.06	0.00	467.30	8.21
SM09-17b	507.73	4	0.08	0.01	0.06	0.02	12.12	0.11	0.06	0.00	551.90	8.65
SM09-17b	746.03	10	0.12	0.01	0.08	0.02	8.03	0.11	0.08	0.00	1057.93	20.11
SM09-17b	974.43	9	0.17	0.01	0.09	0.00	6.02	0.05	0.09	0.00	766.35	10.96
SM09-17b	1205.76	13	0.21	0.01	0.10	0.01	4.77	0.05	0.10	0.00	1104.20	22.55
SM09-17b	1214.78	11	0.21	0.01	0.10	0.01	4.71	0.04	0.10	0.00	1610.63	26.09
SM09-17b	1357.81	12	0.24	0.01	0.11	0.01	4.17	0.04	0.11	0.00	1537.73	20.29
SM09-17b	1368.47	17	0.25	0.01	0.12	0.01	4.07	0.05	0.12	0.00	1076.90	19.15
SM09-17b	1471.61	17	0.26	0.01	0.10	0.01	3.87	0.04	0.10	0.00	1530.94	24.43
SM09-17b	2272.19	22	0.45	0.01	0.19	0.01	2.24	0.02	0.19	0.00	2269.92	31.38
SM09-17b	1053.83	44	0.18	0.04	0.10	0.01	5.48	0.24	0.10	0.00	1526.34	49.41

Table 4. Results of U-Pb zircon dating of the host sandstone (sample TER-R007).

	207 cor 206Pb/238U	*+/-1 ster*	*206Pb/238U*	*+/-1 RSE*	*207Pb/206Pb*	*+/-1 RSE*	*238U/206Pb*	*+/-1 std err*	*207Pb/206Pb*	*+/-1 std err*	*206Pb/238U*	*+/-1 ster*
TER-R007	313.61	5	0.05	0.02	0.06	0.03	19.99	0.33	0.06	0.00	314.64	5.22
TER-R007	319.93	5	0.05	0.02	0.06	0.04	19.47	0.31	0.06	0.00	322.95	5.10
TER-R007	320.88	6	0.05	0.02	0.05	0.02	19.57	0.40	0.05	0.00	321.28	6.52
TER-R007	323.43	5	0.05	0.02	0.05	0.04	19.40	0.32	0.05	0.00	324.05	5.34
TER-R007	347.52	4	0.06	0.01	0.05	0.01	18.04	0.21	0.05	0.00	347.73	4.03
TER-R007	349.41	11	0.06	0.03	0.06	0.04	17.86	0.59	0.06	0.00	351.20	11.57
TER-R007	396.50	5	0.06	0.01	0.06	0.03	15.74	0.21	0.06	0.00	396.95	5.18
TER-R007	431.55	6	0.07	0.01	0.06	0.02	14.42	0.21	0.06	0.00	432.31	6.18
TER-R007	451.91	9	0.07	0.02	0.06	0.02	13.78	0.27	0.06	0.00	451.67	8.81
TER-R007	1498.24	34	0.26	0.02	0.10	0.01	3.81	0.09	0.10	0.00	1501.07	34.93
TER-R007	1549.05	15	0.30	0.01	0.17	0.01	3.39	0.03	0.17	0.00	1667.90	16.32

Table 5. Results of U-Pb zircon dating of the rhyolite (sample SM09-21).

	207 cor 206Pb/238U	*+/-1 ster*	*206Pb/238U*	*+/-1 RSE*	*207Pb/206Pb*	*+/-1 RSE*	*238U/206Pb*	*+/-1 std err*	*207Pb/206Pb*	*+/-1 std err*	*206Pb/238U*	*+/-1 ster*
SM09-21	207.37	3	0.03	0.02	0.05	0.03	30.52	0.49	0.05	0.00	207.85	3.34
SM09-21	215.16	2	0.03	0.01	0.05	0.02	29.43	0.30	0.05	0.00	215.42	2.23
SM09-21	217.23	2	0.03	0.01	0.05	0.01	29.14	0.27	0.05	0.00	217.50	1.99
SM09-21	218.97	2	0.03	0.01	0.05	0.02	28.89	0.31	0.05	0.00	219.34	2.34
SM09-21	219.13	2	0.03	0.01	0.05	0.01	28.90	0.28	0.05	0.00	219.31	2.16
SM09-21	220.01	2	0.03	0.01	0.05	0.02	28.72	0.27	0.05	0.00	220.63	2.04
SM09-21	222.24	2	0.04	0.01	0.05	0.02	28.51	0.28	0.05	0.00	222.26	2.22
SM09-21	227.09	2	0.04	0.01	0.05	0.02	27.81	0.27	0.05	0.00	227.73	2.21
SM09-21	227.43	3	0.04	0.01	0.05	0.02	27.85	0.33	0.05	0.00	227.40	2.68
SM09-21	228.07	2	0.04	0.01	0.06	0.02	27.47	0.27	0.06	0.00	230.50	2.28
SM09-21	228.39	2	0.04	0.01	0.05	0.02	27.75	0.28	0.05	0.00	228.23	2.31
SM09-21	230.78	3	0.04	0.01	0.05	0.02	27.33	0.31	0.05	0.00	231.63	2.66

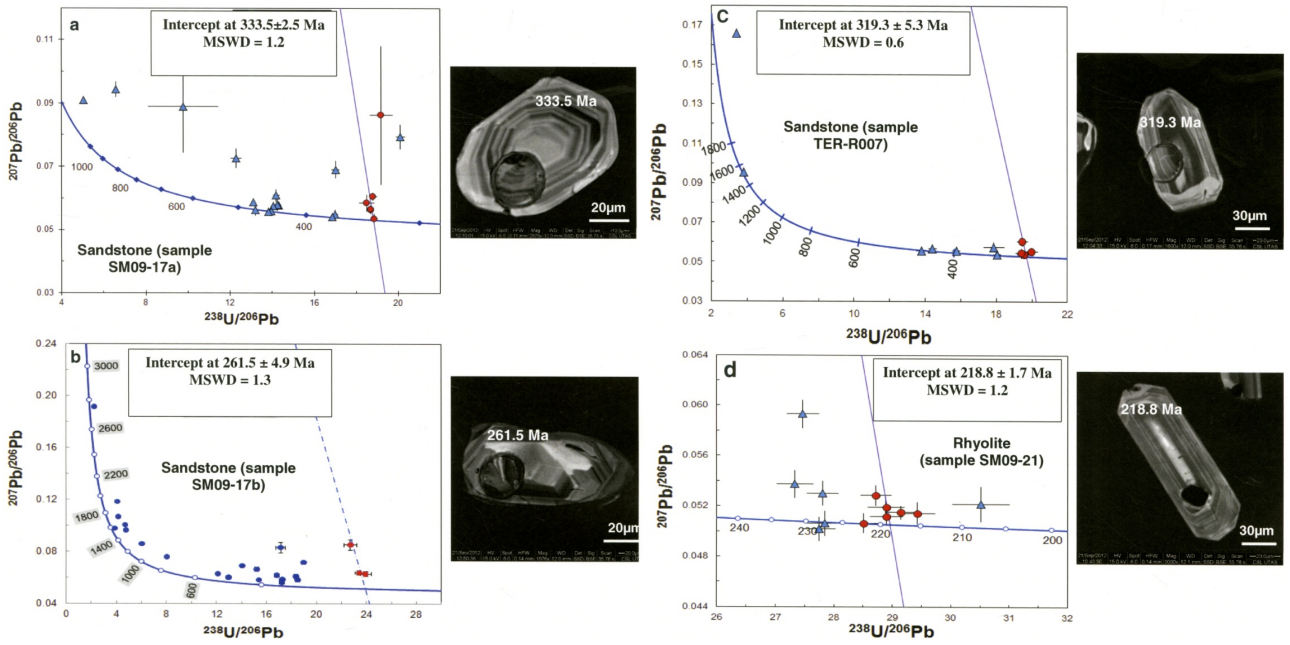

Figure 13. Inverse concordia plots of detrital younger zircon dating for the Tersang gold deposit. The dark, blue and red dots represent the analyzed zircon grains (a) Concordia plot of zircon dating from the host sandstone (sample SM09-17a). (b) Concordia plot of zircon dating from the host sandstone (sample SM09-17b). Inverse concordia plots of detrital younger zircon dating for the Tersang gold deposit. (c) Concordia plot of zircon dating from the host sandstone (sample TER-R007). (d) Concordia plot of zircon dating from the rhyolite (sample SM09-21).

6. Veins and Mineral Occurrence

Two main stages of mineralised quartz veins were found at Tersang. The NNW-SSE trending veins (stage 1) overprinted by the ESE-WNW striking veins (stage 2) (Figure 14a). The stage 1 is characterised by, milky to smoky quartz veins (up to 1.2 m thick) in which pyrite grains are enclosed in sandstone clasts occurring with minor arsenopyrite, sphalerite, rutile, illite and montmorillonite (Figure 14b). This stage represents the earliest vein-fill material and contains up to 90 vol. % of quartz. The sulphide grains account for approximately 10 vol. % of the vein filling. The stage 2 is characterised by the occurrence of free gold, pyrite, arsenopyrite (Figure 14c), galena, geocronite [$Pb_{14}(Sb, As)_6 S_{23}$], covellite, traces of ilmenite, quartz and some silicates (1–5 vol. % of the vein filling). In addition, the stage 2 vein grew syntaxially over periods of cracking and healing followed by precipitation of hematite (Figure 14d) at a late stage (Figures 14e–f). Rutile occurs either in the form of laths or patches in the stage 1 vein (Figure 14b). The patches of rutile are up to 500 µm across and the laths are 10-30 µm wide and 30-40 µm long and are embedded in the silica matrix in stage 1 vein. Hematite occurs in the form of disseminated patches in fractures in the stage 1 vein (Figure 14e). Hematite rims around arsenopyrite crystals in the stage 2 vein.

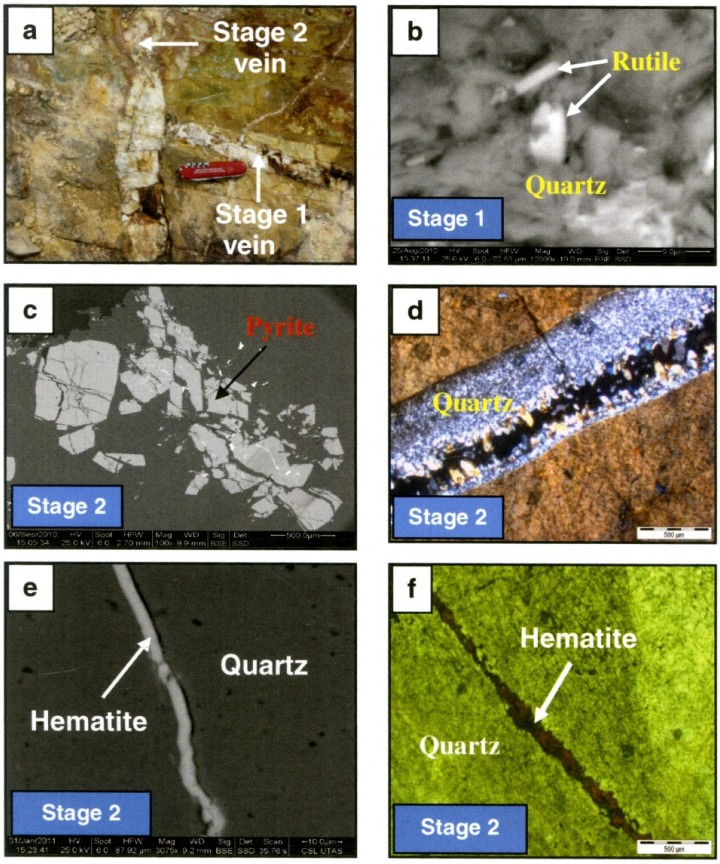

Figure 14. Back-scattered electron images made from ore and gangue minerals at the Tersang gold deposit. (a) The NNW-SSE trending veins (stage 1) overprinted by the ESE-WNW striking veins (stage 2). (b) Rutile in quartz vein (stage 1). (c) Brecciated pyrite in stage 2 vein. (d) Hematite vein grown syntaxially in quartz vein during stage 2. (e) Back-scattered image of hematite vein crosscutting quartz vein in stage 2 vein. (f) Photomicrograph of hematite in stage 2 vein.

In the Tersang gold deposit, the sulphide minerals present are pyrite, arsenopyrite, sphalerite, galena, geocronite, covellite including gold (Figure 15). Gangue minerals are also present including ilmenite, rutile, hematite, illite and montmorillonite. Sulphide minerals occur pervasively in both quartz veins and host rocks whereas clay minerals are only present in quartz veins. Relatively coarse-grained gold particles (20–30 μm) are isolated in the quartz matrix and 2–5 μm grains are locked in arsenopyrite grains (Figure 15), and other gold grains (up to 70 μm) are associated with geocronite.

Gold grains (up to 1 mm) occur at fracture intersections, rimmed by pyrite and arsenopyrite. Arsenopyrite in turn contains 20–50 μm gold inclusions (Figure 15a). Arsenopyrite grains also occur in the form of rhomb-shaped grains ranging from 100 to 200 μm wide. In addition, some arsenopyrite grains are broken, which sizes are 50 to 100 μm wide (Figure 15b). It also rims pyrite grains in veins and sometimes occurs as isolated grains, with size ranges from 200 to 400 μm. Some 2–5 μm wide gold veins were found in fractured arsenopyrite grains. Up to 300 μm wide, subhedral, arsenopyrite grains also occur in the stage 2 quartz veins. Sphalerite occurs as large (up to 1 mm across) patches

in the stage 1 vein and found together with arsenopyrite and galena (Figure 15c). Galena occurs in the form of tiny inclusions less than 10 µm in size in sphalerite.

Galena is found in most of the samples collected from the stage 2 quartz veins. The grains are up to 1 mm across and occur in fractures associated with arsenopyrite and pyrite. Galena also occurs in the form of larger patches around arsenopyrite (Figure 15d). In addition, galena occurs as isolated veinlets that thickness varies from 5 to 10 µm. It also occurs as inclusions in sphalerite grains. Geocronite was newly identified using the electron probe micro-analyser (Figure 15e). The less than 1mm wide geocronite grain was found using the scanning electron microscope. It fills fractures in quartz veins, and associated with euhedral pyrite in stage 2 vein (Figure 15e). Covellite was found by electron microprobe analysis and occurs in fractures where it partly replaces galena in the stage 2 veins (Figure 15f).

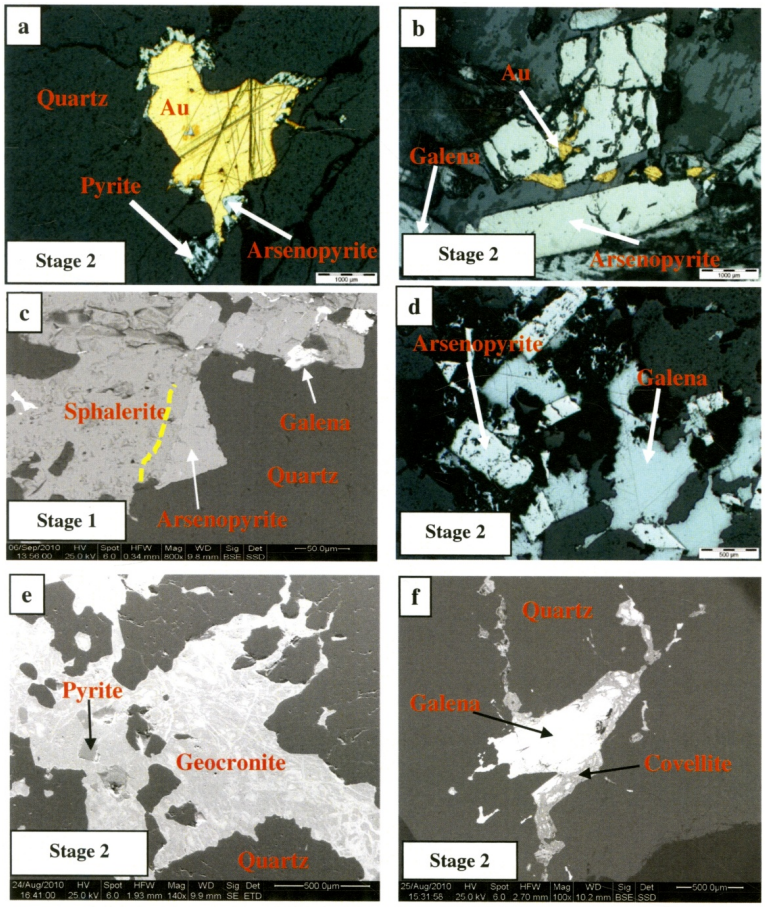

Figure 15. Ore minerals present at the Tersang gold deposit. (a) Free gold associated with pyrite and arsenopyrite in quartz-sulphide vein (sample TER-R035). (b) Free gold in quartz-sulphide vein (sample TER-R042). (c) Back-scattered electron image of sphalerite, arsenopyrite and galena (sample TER-R008). (d) Galena and arsenopyrite in quartz-sulphide vein (sample TER-R029). (e) Back-scattered electron image of geocronite and euhedral pyrite 1 (sample TER-R030). (f) Back-scattered electron image of galena associated with covellite (sample TER-R041).

Pyrite predominantly occurs as euhedral to subhedral or aggregate grains (Figures 16a–g) in the fine-grained sandstone. These pyrite grains and aggregate have also been found in host rock bits embedded in quartz veins. Euhedral to subhedral pyrite grains, up to 300 μm wide, have porous cores in the sandstone (Figures 16a, c, and d). Pyrite grains (50 to 100 μm across) are also characterised by the presence of internal fracturing in phases 2 and 3. This type of pyrite is mostly disseminated in the host sandstone with a < 20 μm thick discontinuous rim (Figure 16). The pyrite aggregates are 250–500 μm wide in the host sandstone. The stage 2 vein-hosted pyrite grains are euhedral to subhedral, internally fractured, up to 1 mm in width.

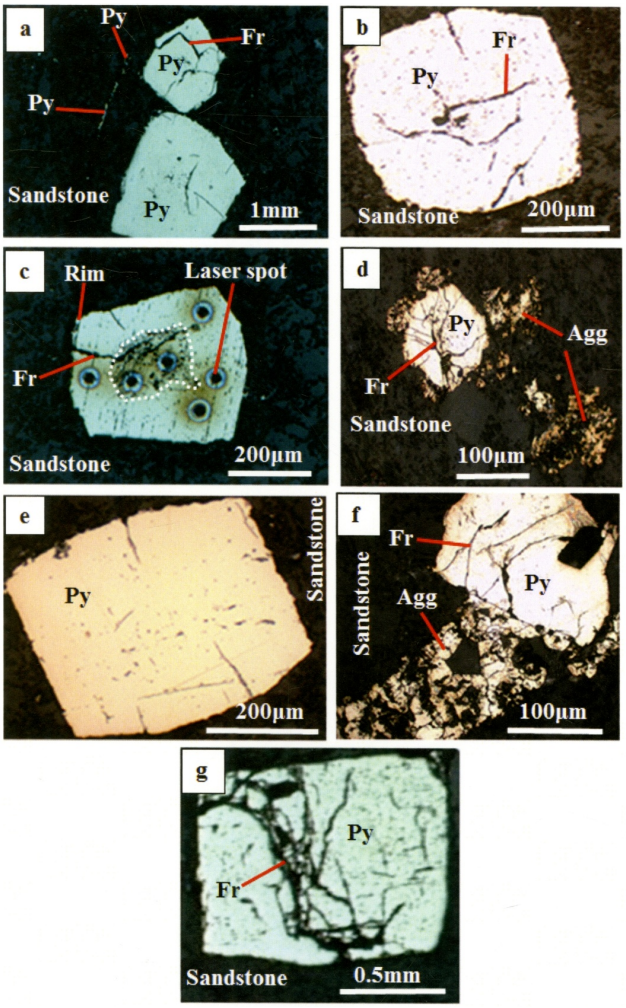

Figure 16. Textural characteristics of pyrite recorded at the Tersang gold deposit. (a) Subhedral pyrite in host sandstone (sample TER-R007). (b) Euhedral clean pyrite with fractures from sandstone (sample TER-R007). (c) Euhedral clean pyrite with porous core from sandstone (sample TER-R007). (d) Euhedral and aggregate pyrite from sandstone (sample TER-R007). (e) Euhedral pyrite from sandstone clasts in quartz veins (sample TER-R039). (f) Euhedral and aggregate pyrite from sandstone (sample TER-007). (g) Euhedral pyrite with internal fracturing from sandstone pieces in quartz veins (sample TER-R039).

7. Pyrite Analyses

A total of seven Laser Ablation ICPMS maps of pyrite grains and aggregates (Figures 2–8) were made from pyritic sandstone (host rocks) collected from the open pit at Tersang. In this study, vein-hosted pyrite grains in the stages 1 and 2 veins were oxidized due to weathering and they were not mapped to investigate their trace element composition.

Results of pyrite trace element compositions include maximum, minimum detection limit, mean, and standard deviation are presented in Table 6. The controls on nucleation and growth of the pyrite grains was not an easy task to work out from pyrite morphology; however, the pyrite mapping has helped distinguish four pyrite phases shown by the distribution of some elements such as Te, Bi, As, Au, Pb, Co, and Ni within the pyrite structure (Figures 2–8). These trace elements show some zonation patterns on pyrite maps (Figures 2–8). Gold pixel images were useful to distinguish four pyrite phases 1, 2, 3 and 4 (Figures 2–8). Pyrite phase 1 contains U-rich and Sb-rich inclusions, Pb-rich (galena) inclusions and Zn-rich (sphalerite) inclusions (Figures 2–5; 7). This pyrite phase contains (a) high levels of As, Co, Ni, Ti, Sb and Se (b) minor levels of Cu, Zn, Pb, Bi, Te, Ag, Tl, W, V and (c) traces of Mo, Pt (Tables 6A-B; Figures 2–5). Gold levels were detected ranging from 0.08 to 20.5 ppm Au (mean 0.7 ppm). The anomalous trace element compositions range from 1,438 to 15,187.5 ppm As (mean 6,250.6 ppm), 0.01 to 144,733.5 ppm Ti (mean 803 ppm), 0.01 to 1,340 ppm Ni (mean 121.4 ppm) and 0.01 to 2,580.4 ppm Co (mean 117.6 ppm).

Pyrite phase 2 contains inclusions enriched in Ti (rutile), As (arsenopyrite), Cu (chalcopyrite) and Pb (galena) (Figures 2–5). Other inclusions are silicates, Ag-rich inclusions, Sb-rich inclusions, and W-rich inclusions (Table 6A-B; Figures 2–5; 7). The Ag-Cu enriched inclusions are mostly present in the rim (Figure 7). A Mo-rich inclusion has also been found at the boundary between pyrite phases 1 and 2 (Figure 7). This pyrite phase is characterised by (a) high levels of As, Sb, Ti, Co, Ni, Se, Cu (b) minor levels of Au, Pb, Tl, V, Bi, Zn, W (c) trace amounts of Ag, Te, Pt, and Mo (Table 6A and B; Figures 2–5 and 7). Detected levels of gold vary from 0.01 to 99.3 ppm Au (mean 4.6 ppm). The anomalous trace element compositions range from 355 to 46,277.6 ppm As (mean 17,035.8 ppm), 0.01 to 76,403 ppm Ti (mean 1157 ppm), 0.01 to 1,731 ppm Ni (mean 131 ppm), and 0.01 to 2,126.5 ppm Co (mean 77.6 ppm).

Pyrite phase 3 shows Co-Ni zoning patterns and numerous Ti-rich inclusions and V-rich inclusions (Figures 2–5). This pyrite phase contains (a) high levels of As, Se, Co, Ni, Tl, Sb (b) minor levels of Cu, Zn, V, W, Au, Pb (c) traces of Bi, Mo, Ag, Te, and Pt. Gold concentrations vary from 0.01 to 223.5 ppm (mean 1.5 ppm). The anomalous trace element compositions range from 7.7 to 15,187.3 ppm As (mean 7291 ppm), 0.01 to 146398.7 ppm Ti (mean 1400.3 ppm), 0.01 to 1572 ppm Co (mean 106 ppm), and 0.01 to 1762.3 ppm Ni (mean 138 ppm).

Pyrite phase 4 is characterised by the presence of Cu, Tl, and Zn-rich inclusions (Figures 2–5; 7). This pyrite phase consists of (a) elevated levels of As, Ti, Ni, Co, Zn, W, Se, Tl; (b) minor levels of Au, V, and Cu; (c) trace amounts of Mo, Pt, Ag, and Te (Tables 6A-B). Gold concentrations vary from 0.01 to 15 ppm (mean 0.5 ppm). The anomalous trace element compositions range from 30 to 10622 ppm As (mean 2802 ppm), 0.01 to 101,784 ppm Ti (mean 1342 ppm), and 0.01 to 1281 ppm Ni (mean 73 ppm).

Table 6A. LA-ICPMS analyses of pyrite mapping at the Tersang gold deposit, Malaysia.

Pyrite phase	*Co*	*Ni*	*Ti*	*V*	*Cu*	*Zn*	*As*	*Se*	*Mo*
Phase 1: High Te_ Sb_ Bi : Minimum	0.01	0.01	0.01	0.01	0.01	0.01	1438.13	1.11	0.01
Phase 1: High Te_ Sb_ Bi : Maximum	2580.42	1340.05	144733.51	471.88	878.07	8071.16	15187.53	1018.98	5.19
Phase 1: High Te_ Sb_ Bi : Mean	117.65	121.44	802.83	3.97	14.79	18.47	6250.59	25.40	0.02
Phase 1: High Te_ Sb_ Bi : Median	44.09	65.01	28.15	0.01	3.54	1.12	6317.82	6.96	0.01
Phase 1: High Te_ Sb_ Bi : Standard Deviation	200.88	165.88	4504.35	16.18	31.15	274.08	2283.28	74.89	0.16
Phase 1: High Te_ Sb_ Bi : Interquartile Range	145.83	143.26	261.88	0.88	14.32	2.46	3177.86	11.50	0.00
Phase 2: High As_ Au and Sb : Minimum	0.01	0.01	0.01	0.01	0.01	0.01	355.03	1.11	0.01
Phase 2: High As_ Au and Sb : Maximum	2126.50	1730.86	76403.04	326.63	34680.84	4153.23	46277.60	1197.12	28.58
Phase 2: High As_ Au and Sb : Mean	77.58	130.84	1156.85	4.31	40.40	3.34	17035.84	47.32	0.03
Phase 2: High As_ Au and Sb : Median	7.52	32.50	29.36	0.10	2.77	0.03	8557.27	11.67	0.01
Phase 2: High As_ Au and Sb : Standard Deviation	160.30	213.55	4660.91	12.17	574.94	60.97	34749.75	140.85	0.47
Phase 2: High As_ Au and Sb : Interquartile Range	75.32	167.89	308.94	3.17	4.67	1.02	4323.44	10.83	0.00
Phase 3: Low Au_ Sb_ Pb : Minimum	0.01	0.01	0.01	0.01	0.01	0.01	7.76	1.11	0.01
Phase 3: Low Au_ Sb_ Pb : Maximum	1571.93	1762.27	146398.66	271.26	527.58	14076.02	15187.30	1089.65	2.48
Phase 3: Low Au_ Sb_ Pb : Mean	105.70	137.99	1400.28	3.65	10.69	9.24	7290.76	25.68	0.01
Phase 3: Low Au_ Sb_ Pb : Median	32.35	63.99	13.16	0.01	2.77	0.03	5216.75	11.67	0.01
Phase 3: Low Au_ Sb_ Pb : Standard Deviation	166.75	197.78	7218.96	13.45	35.75	272.46	10636.03	71.09	0.04
Phase 3: Low Au_ Sb_ Pb : Interquartile Range	128.15	162.08	289.58	0.60	0.32	0.16	3974.68	9.31	0.00
Phase 4: Low As_ Co_ and Ni : Minimum	0.01	0.01	0.01	0.01	0.01	0.01	29.91	1.11	0.01
Phase 4: Low As_ Co_ and Ni : Maximum	928.99	1281.13	101783.78	145.54	878.07	15127.39	10621.59	174.13	2.74
Phase 4: Low As_ Co_ and Ni : Mean	52.68	72.09	1342.12	5.37	8.13	43.91	2801.64	12.98	0.02
Phase 4: Low As_ Co_ and Ni : Median	12.85	31.99	13.16	0.01	2.77	0.02	2512.27	11.67	0.01
Phase 4: Low As_ Co_ and Ni : Standard Deviation	97.88	108.19	5766.03	14.89	22.91	655.10	1668.34	15.21	0.12
Phase 4: Low As_ Co_ and Ni : Interquartile Range	38.72	71.80	340.31	2.15	0.32	0.01	2046.17	5.35	0.00

Table 6B. LA-ICPMS spot analyses of pyrite at the Tersang gold deposit, Malaysia.

Pyrite phase	*Ag*	*Sb*	*Te*	*W*	*Pt*	*Au*	*Tl*	*Pb*	*Bi*
Phase 1: High Te_ Sb_ Bi : Minimum	0.01	0.01	0.01	0.01	0.01	0.08	0.01	0.01	0.01
Phase 1: High Te_ Sb_ Bi : Maximum	69.30	2516.13	10.17	1499.88	1.91	20.52	144.91	274.86	25.88
Phase 1: High Te_ Sb_ Bi : Mean	0.78	43.80	0.49	4.76	0.04	0.77	1.32	10.03	0.38
Phase 1: High Te_ Sb_ Bi : Median	0.01	8.45	0.26	0.01	0.01	0.48	0.01	4.31	0.18
Phase 1: High Te_ Sb_ Bi : Standard Deviation	3.88	111.70	0.78	43.04	0.05	0.89	5.37	16.95	1.03
Phase 1: High Te_ Sb_ Bi : Interquartile Range	0.23	33.72	0.43	0.72	0.06	0.76	0.07	11.92	0.34
Phase 2: High As_ Au and Sb : Minimum	0.01	0.01	0.01	0.01	0.01	0.01	0.01	0.01	0.01
Phase 2: High As_ Au and Sb : Maximum	784.93	33036.18	20.76	1113.89	3.45	99.36	622.46	4144.54	62.24
Phase 2: High As_ Au and Sb : Mean	0.94	147.31	0.26	5.07	0.04	4.57	4.10	15.90	1.19
Phase 2: High As_ Au and Sb : Median	0.01	6.61	0.07	0.01	0.01	2.53	0.01	5.06	0.01
Phase 2: High As_ Au and Sb : Standard Deviation	13.68	739.25	0.64	30.16	0.08	6.67	22.94	71.62	2.82
Phase 2: High As_ Au and Sb : Interquartile Range	0.00	26.50	0.39	0.00	0.06	4.52	0.00	18.33	0.67
Phase 3: Low Au_ Sb_ Pb : Minimum	0.01	0.01	0.01	0.01	0.01	0.01	0.01	0.01	0.01
Phase 3: Low Au_ Sb_ Pb : Maximum	23.15	2440.94	10.17	1876.38	1.62	223.53	555.42	871.22	12.87
Phase 3: Low Au_ Sb_ Pb : Mean	0.12	38.73	0.24	12.40	0.04	1.48	2.64	4.43	0.24
Phase 3: Low Au_ Sb_ Pb : Median	0.01	1.12	0.07	0.01	0.03	0.48	0.01	0.01	0.01
Phase 3: Low Au_ Sb_ Pb : Standard Deviation	0.84	157.06	0.68	78.06	0.05	5.73	16.81	24.48	0.83
Phase 3: Low Au_ Sb_ Pb : Interquartile Range	0.00	4.84	0.39	1.33	0.06	1.39	0.00	2.76	0.00
Phase 4: Low As_ Co_ and Ni : Minimum	0.01	0.01	0.01	0.01	0.01	0.01	0.01	0.01	0.01
Phase 4: Low As_ Co_ and Ni : Maximum	5.20	1398.86	9.80	769.55	1.03	14.94	72.09	186.99	6.93
Phase 4: Low As_ Co_ and Ni : Mean	0.08	31.01	0.18	14.29	0.04	0.51	1.58	4.43	0.12
Phase 4: Low As_ Co_ and Ni : Median	0.01	2.54	0.01	0.01	0.01	0.09	0.01	0.01	0.01
Phase 4: Low As_ Co_ and Ni : Standard Deviation	0.36	86.04	0.44	59.92	0.05	0.98	5.00	12.55	0.52
Phase 4: Low As_ Co_ and Ni : Interquartile Range	0.00	18.79	0.39	1.06	0.06	0.45	0.35	4.31	0.00

8. Discussion

Laser Ablation ICPMS pyrite mapping has revealed four chemically distinct pyrite phases, namely pyrite phases 1, 2, 3, and 4 (Table 7). The Ag/Au ratio values have been used to infer the origin of each pyrite phase [18,32,2]. Previous research documented that diagenetic/syngenetic pyrites have Ag/Au > 1, whereas metamorphic-hydrothermal pyrites have Ag/Au < 1. In this study, pyrite phase 1 is characterized by elevated levels of V, As, Mo, Se, Ni, Ag, and Zn, with Ag/Au mean value of 1.01.

Table 7. Chemical characteristics of pyrite phases at the Tersang gold deposit, Malaysia.

	Pyrite phase 1	***Pyrite phase***	***Pyrite phase 3***	***Pyrite phase 4***
High levels of trace element	As, Co, Ni, Ti, Sb, Se	As, Sb, Ti, Co, Ni, Se, Cu	As, Co, Ni, Tl, Sb, Se	As, Se, Co, Tl, Ti, Zn, W
Low levels of trace element	Cu, Zn, Pb, Bi, Te, Ag, Tl, W, V	Au, Pb, Te, V, Bi, Zn, W	Cu, Zn, V, W, Au, Pb	Au, V, Cu
Traces	Mo, Pt	Ag, Mo, Pt	Bi, Mo, Ag, Te, Pt	Ag, Te, Mo, Pt
Gold content (ppm)	0.08<Au<20.5	0.01<Au<99.3	0.01<Au<223.5	0.01<Au<15
Inclusions	Chalcopyrite, sphalerite	Arsenopyrite, galena, chalcopyrite	Rutile	Chalcopyrite, sphalerite

The Ag/Au ratio mean values of pyrite phases 2, 3, and 4 are 0.2, 0.08 and 0.15 respectively. The evidence indicates that the Ag/Au ratios for pyrite phases 2, 3, and 4 are much lower compared to that of pyrite phase 1. Pyrite phase 1 likely formed from a diagenetic fluid; whereas pyrite phases 2, 3, and 4 may have formed from metamorphic-hydrothermal fluids. Referring to the work of Kolker [33,34], the common range of arsenic content in sedimentary pyrites in the Mississippian Marshall sandstone of south eastern Michigan in USA varies from 0 to 1 wt% (10,000 ppm). Additionally, the arsenic content in hydrothermal pyrites ranges from 0.001 to 10 wt% (100,000 ppm).

In light with the present study, it turns out that pyrite phases 2, 3, and 4 have elevated As values implying their hydrothermal origin. The pyrite phases indicate temporal and chemical variations during crystallisation of ore forming fluids. Pyrite phase 1 represents the core zones of most euhedral pyrite grains, and contains elevated matrix content and low gold concentrations (mean 0.4 ppm). It is interpreted as the pre-main Au stage in the pyrite generations in the Tersang gold deposit. Pyrite phases 2 and 3 are interpreted to be the main gold stage with mean values ranging from 1.5 to 4.5 ppm Au. Pyrite phase 4 postdates the main Au stage (pyrite phases 2 and 3) with a mean value of 0.5 ppm Au because it is the pyrite phase that is present along the rims or margins. The evidence indicates that there is variation of gold concentration reflected by a differing

chemistry (pyrite phases 1–4) of the ore-forming fluids. In all the pyrite phases, gold correlate positively with trace elements (Tables 8A–D) such as As, Cu, Pb, Ag, Sb, Tl, Se (Figure 17). Coefficients of correlations (cc) vary from 0.27 to 0.72. Tl shows a particularly strong correlation with Au (cc = 0.72). The trace metals that correlate well with gold, may serve as chemical vectors for proximity to gold mineralisation in the Tersang mineral district. Most gold (or refractory gold) in the pyrite phases 1–4 occurs in the pyrite lattice (Figure 18). Three analysed points (free gold) plot above the saturation line of Reich [35] implying the existence of gold in the form of micro inclusions in pyrite phase 3 (Figure 18). The pyrite phase data are not confined within the Carlin Sediment-Hosted Gold Deposit (SHGD) field (the yellow dotted polygon) indicating a poor affinity with the SHGD-style deposits (Figure 18). Trace element contents in pyrite phases 1, 2, 3, and 4 display broadly two trends: The first trend is that of those trace elements, which concentrations vary tremendously over time including Co, Ni, Ti, Zn, As, Sb, Te, V, Au, Pb, Bi, and Tl. The second trend is for trace elements, which contents do not change much through time and consist of Cu, Mo, Ag, Pt, and Se (Figures 19,20).

Laser Ablation ICPMS analyses on pyrite has shown that pyrite phase 1 has low Au concentration (mean 0.4 ppm) and is interpreted to have preceded the main Au mineralisation event (phase 3). Overall, pyrite phases 2 and 3 are the main Au mineralisation stages with Au mean range from 1.5 to 4.5 ppm and significantly contributed the amount of invisible gold to the ore-forming system at Tersang. Pyrite phase 4 has low gold levels (mean 0.5 ppm) and post-dated the main Au mineralisation stage (pyrite phases 2 and 3). The evidence suggests that the distribution of gold in diagenetic pyrite phase 1 and metamorphic-hydrothermal pyrite phases 2, 3, and 4 likely testify the result of four stages ore-forming system centred on the rhyolite corridor in the Tersang gold deposit. Most gold was sourced from metamorphic-hydrothermal fluids.

In the Jugan gold deposit [36], As and Tl were utilised as pathfinders to Au mineralisation indicating similarity to the Tersang gold deposit. Back-scattered electron images showed a significant amount of fractured pyrite, arsenopyrite and sphalerite grains, which suggest that sulphide grains have been subjected to brittle deformation. Numerous broken arsenopyrite grains, which contain free gold in its cracks probably, indicate circulation of ore-forming fluids through the cracks in arsenopyrite during deformation. Regionally, lode or quartz stockwork-style mineralisation is known to contain economic Au mineralisation and they have been explored and mined in different locations in mainland Southeast Asia.

Stratigraphically, our new data implies a Carboniferous maximum depositional age of the underlying sandstone unit (oldest sandstone horizon) and possibly a Permian maximum depositional age for the overlying sandstone unit (youngest sandstone layer) in the deposit. Additionally, the crystallisation age of the volcanic rock (rhyolite) is 218.8 ± 1.7 Ma indicating magmatism in the Late Triassic. This age of the rhyolite also provides a minimum age for the sandstone, possibly ranging from 262 to 219 Ma.

Table 8A. Pearson correlation matrix of trace elements in pyrite phase 1 at the Tersang gold deposit, Malaysia.

	Co	*Ni*	*Ti*	*V*	*Cu*	*Zn*	*As*	*Se*	*Mo*	*Ag*	*Sb*	*Te*	*W*	*Pt*	*Au*	*Tl*	*Pb*	*Bi*
Co	1	0.71	0.04	-0.097	-0.11	-0.0016	0.12	-0.12	-0.0053	-0.029	-0.14	-0.11	-0.0017	-0.12	-0.059	-0.13	0.0032	0.046
Ni	0.71	1	-3.04	-0.13	-0.14	-0.021	0.25	-0.13	-0.015	-0.055	-0.19	-0.025	-0.021	-0.037	-0.018	-0.15	-0.042	0.031
Ti	0.04	-3.00	1	0.52	-0.0046	-0.0051	-0.066	-0.029	-0.0068	2.80E-05	-0.011	0.0076	0.9	-0.028	0.029	-0.016	0.023	0.039
V	-0.097	-0.13	0.52	1	0.19	-0.015	-0.0089	0.078	-0.013	-0.037	0.21	0.29	0.51	0.23	-0.017	0.19	0.016	-0.012
Cu	-0.11	-0.14	-0.0046	0.19	1	0.059	0.14	0.25	0.0058	0.25	0.46	0.25	-0.011	0.26	0.34	0.46	0.29	0.057
Zn	-0.0016	-0.021	-0.0051	-0.015	0.059	1	-0.013	-0.015	-4.70E-04	0.11	-0.0095	-0.024	-0.0018	0.045	0.016	-0.015	0.05	0.021
As	0.12	0.25	-0.066	-0.0089	0.14	-0.013	1	0.11	-0.0049	-0.037	0.024	0.16	-0.076	0.12	0.17	0.063	0.037	0.06
Se	-0.12	-0.13	-0.029	0.078	0.25	-0.015	0.11	1	-0.012	-0.024	0.43	0.2	-0.016	0.23	0.068	0.47	0.0091	-0.044
Mo	-0.0053	-0.015	-0.0068	-0.013	0.0058	-4.70E-04	-0.0049	-0.012	1	0.023	-0.0043	0.028	-0.0048	-0.024	0.024	-0.011	0.047	0.13
Ag	-0.029	-0.055	2.80E-05	-0.037	0.25	0.11	-0.037	-0.024	0.023	1	0.014	-0.027	-0.0062	0.019	0.27	-0.015	0.22	0.089
Sb	-0.14	-0.19	-0.011	0.21	0.46	-0.0095	0.024	0.43	-0.0043	0.014	1	0.34	-0.0044	0.27	0.17	0.64	0.23	0.014
Te	-0.11	-0.025	0.0076	0.29	0.25	-0.024	0.16	0.2	0.028	-0.027	0.34	1	0.015	0.43	-0.032	0.23	0.087	0.21
W	-0.0017	-0.021	0.9	0.51	-0.011	-0.0018	-0.076	-0.016	-0.0048	-0.0062	-0.0044	0.015	1	-0.011	0.01	-0.0081	0.0017	0.011
Pt	-0.12	-0.037	-0.028	0.23	0.26	0.045	0.12	0.23	-0.024	0.019	0.27	0.43	-0.011	1	0.0024	0.23	0.027	-0.02
Au	-0.059	-0.018	0.029	-0.017	0.34	0.016	0.17	0.068	0.024	0.27	0.17	-0.032	0.01	0.0024	1	0.14	0.27	0.081
Tl	-0.13	-0.15	-0.016	0.19	0.46	-0.015	0.063	0.47	-0.011	-0.015	0.64	0.23	-0.0081	0.23	0.14	1	0.16	-0.039
Pb	0.0032	-0.042	0.023	0.016	0.29	0.05	0.037	0.0091	0.047	0.22	0.23	0.087	0.0017	0.027	0.27	0.16	1	0.22
Bi	0.046	0.031	0.039	-0.012	0.057	0.021	0.06	-0.044	0.13	0.089	0.014	0.21	0.011	-0.02	0.081	-0.039	0.22	1

Table 8B. **Pearson correlation matrix of trace elements in pyrite phase 2 at the Tersang gold deposit, Malaysia.**

	Co	*Ni*	*Ti*	*V*	*Cu*	*Zn*	*As*	*Se*	*Mo*	*Ag*	*Sb*	*Te*	*Au*	*Tl*	*Pb*	*Bi*
Co	1	0.76	0.077	-0.081	-0.03	0.002	-0.11	-0.1	-0.014	-0.027	-0.09	-0.059	-0.17	-0.084	-0.078	-0.13
Ni	0.76	1	0.055	-0.12	-0.034	-0.0098	-0.14	-0.13	-0.018	-0.034	-0.11	-0.069	-0.2	-0.11	-0.067	-0.16
Ti	0.077	0.055	1	0.42	-0.011	0.0071	-0.042	-0.053	-0.0031	-0.012	-0.033	-0.032	-0.05	-0.031	0.018	0.14
V	-0.081	-0.12	0.42	1	0.014	-0.0066	0.055	0.038	-0.009	-0.0075	0.038	0.13	-0.0029	0.058	0.076	0.2
Cu	-0.03	-0.034	-0.011	0.014	1	0.01	0.078	0.079	0.0021	0.88	0.77	0.027	0.046	0.087	0.11	0.12
Zn	0.002	-0.0098	0.0071	-0.0066	0.01	1	0.041	0.028	0.0047	0.015	0.028	-0.0034	0.032	0.019	-0.0023	-0.014

As	-0.11	-0.14	-0.042	0.055	0.078	0.041	1	0.47	0.034	0.025	0.4	0.17	0.39	0.34	0.032	-0.043
Se	-0.1	-0.13	-0.053	0.038	0.079	0.028	0.47	1	0.044	0.059	0.57	0.14	0.53	0.7	0.058	-0.09
Mo	-0.014	-0.018	-0.0031	-0.009	0.0021	0.0047	0.034	0.044	1	0.0042	0.031	-0.0033	0.025	0.024	-0.0015	-0.01
Ag	-0.027	-0.034	-0.012	-0.0075	0.88	0.015	0.025	0.059	0.0042	1	0.7	-0.00073	0.068	0.11	0.011	0.092
Sb	-0.09	-0.11	-0.033	0.038	0.77	0.028	0.4	0.57	0.031	0.7	1	0.076	0.36	0.47	0.053	0.042
Te	-0.059	-0.069	-0.032	0.13	0.027	-0.0034	0.17	0.14	-0.0033	-0.00073	0.076	1	0.082	0.067	0.059	0.02
W	0.068	0.034	0.63	0.43	-0.0062	0.01	-0.02	-0.033	0.0065	-0.0043	-0.019	-0.02	-0.038	-0.016	0.0077	0.085
Pt	-0.024	-0.046	0.0028	0.082	0.005	-0.0018	0.07	0.098	-0.0028	-0.0062	0.047	0.064	0.031	0.047	0.0027	-0.015
Au	-0.17	-0.2	-0.05	-0.0029	0.046	0.032	0.39	0.53	0.025	0.068	0.36	0.082	1	0.56	0.052	0.037
Tl	-0.084	-0.11	-0.031	0.058	0.087	0.019	0.34	0.7	0.024	0.11	0.47	0.067	0.56	1	0.066	-0.058
Pb	-0.078	-0.067	0.018	0.076	0.11	-0.0023	0.032	0.058	-0.0015	0.011	0.053	0.059	0.052	0.066	1	0.39
Bi	-0.13	-0.16	0.14	0.2	0.12	-0.014	-0.043	-0.09	-0.01	0.092	0.042	0.02	0.037	-0.058	0.39	1

Table 8C. Pearson correlation matrix of trace elements in pyrite phase 3 at the Tersang gold deposit, Malaysia.

	Co	**Ni**	**Ti**	**V**	**Cu**	**Zn**	**As**	**Se**	**Mo**	**Ag**	**Sb**	**Te**	**Au**	**Tl**	**Pb**	**Bi**
Co	1	0.78	0.091	-0.0014	-0.13	0.011	-0.051	-0.1	-0.0057	-0.072	-0.14	0.013	-0.045	-0.095	-0.056	0.02
Ni	0.78	1	0.039	-0.048	-0.13	0.013	-0.023	-0.11	-0.0057	-0.079	-0.15	0.024	-0.046	-0.1	-0.048	0.067
Ti	0.091	0.039	1	0.76	0.0048	0.007	0.012	-0.027	0.004	-0.0089	0.0076	-0.0035	-0.0062	-0.014	0.058	0.16
V	-0.0014	-0.048	0.76	1	0.26	-0.0041	0.091	0.12	0.0022	0.16	0.27	0.1	0.16	0.2	0.14	0.14
Cu	-0.13	-0.13	0.0048	0.26	1	-0.001	0.53	0.35	0.062	0.32	0.57	0.28	0.12	0.31	0.33	0.11
Zn	0.011	0.013	0.007	-0.0041	-0.001	1	-0.0052	-0.0076	4.20E-04	0.013	-0.0023	-0.0069	-0.0037	-0.0043	0.0052	0.012
As	-0.051	-0.023	0.012	0.091	0.53	-0.0052	1	0.16	0.051	0.05	0.32	0.1	-0.0056	0.12	0.35	0.24
Se	-0.1	-0.11	-0.027	0.12	0.35	-0.0076	0.16	1	0.0074	0.51	0.67	0.078	0.36	0.49	0.064	-0.018
Mo	-0.0057	-0.0057	0.004	0.0022	0.062	4.20E-04	0.051	0.0074	1	0.0065	0.028	-0.0035	-0.0015	0.051	0.011	0.025
Ag	-0.072	-0.079	-0.0089	0.16	0.32	0.013	0.05	0.51	0.0065	1	0.75	-0.0071	0.59	0.42	0.075	0.02
Sb	-0.14	-0.15	0.0076	0.27	0.57	-0.0023	0.32	0.67	0.028	0.75	1	0.093	0.62	0.71	0.19	0.05
Te	0.013	0.024	-0.0035	0.1	0.28	-0.0069	0.1	0.078	-0.0035	-0.0071	0.093	1	-0.028	0.044	0.086	-0.0034
W	0.057	0.017	0.87	0.75	0.012	6.80E-04	0.022	-0.019	0.015	-0.0076	0.013	-2.00E-04	-0.01	-0.0091	0.051	0.11
Pt	-0.12	-0.14	-0.031	0.016	0.17	-0.017	0.024	0.022	-0.0045	-0.022	0.024	0.059	-0.072	-0.023	0.03	-0.033
Au	-0.045	-0.046	-0.0062	0.16	0.12	-0.0037	-0.0056	0.36	-0.0015	0.59	0.62	-0.028	1	0.72	0.015	-4.70E-04
Tl	-0.095	-0.1	-0.014	0.2	0.31	-0.0043	0.12	0.49	0.051	0.42	0.71	0.044	0.72	1	0.069	-0.0017

Pb	-0.056	-0.048	0.058	0.14	0.33	0.0052	0.35	0.064	0.011	0.075	0.19	0.086	0.015	0.069	1	0.33
Bi	0.02	0.067	0.16	0.14	0.11	0.012	0.24	-0.018	0.025	0.02	0.05	-0.0034	-4.70E-04	-0.0017	0.33	1

Table 8D. **Pearson correlation matrix of trace elements in pyrite phase 4 at the Tersang gold deposit, Malaysia.**

	Co	***Ni***	***Ti***	***V***	***Cu***	***Zn***	***As***	***Se***	***Mo***	***Ag***	***Sb***	***Te***	***Au***	***Tl***	***Pb***	***Bi***
Co	1	0.81	0.061	-0.063	-0.068	0.05	0.56	-0.02	0.008	-0.012	-0.1	0.065	0.068	-0.071	0.053	0.13
Ni	0.81	1	0.026	-0.1	-0.064	0.05	0.6	-0.025	0.016	0.0084	-0.1	0.043	0.12	-0.061	0.09	0.13
Ti	0.061	0.026	1	0.65	0.026	-0.0027	-0.029	-0.015	0.017	0.026	0.05	0.03	0.044	-0.0075	0.11	0.1
V	-0.063	-0.1	0.65	1	0.18	-0.01	-0.29	0.072	0.0011	0.1	0.18	0.032	0.11	0.09	0.073	0.063
Cu	-0.068	-0.064	0.026	0.18	1	0.063	-0.16	0.35	0.23	0.48	0.44	0.01	0.47	0.41	0.35	0.14
Zn	0.05	0.05	-0.0027	-0.01	0.063	1	0.0092	0.017	0.1	0.12	0.036	-0.0073	0.1	0.11	0.14	0.093
As	0.56	0.6	-0.029	-0.29	-0.16	0.0092	1	-0.026	-0.019	-0.096	-0.26	0.041	0.11	-0.2	-0.05	0.078
Se	-0.02	-0.025	-0.015	0.072	0.35	0.017	-0.026	1	0.12	0.25	0.27	0.0088	0.34	0.27	0.16	0.069
Mo	0.008	0.016	0.017	0.0011	0.23	0.1	-0.019	0.12	1	0.3	0.089	0.0026	0.19	0.11	0.41	0.13
Ag	-0.012	0.0084	0.026	0.1	0.48	0.12	-0.096	0.25	0.3	1	0.27	0.031	0.48	0.28	0.47	0.2
Sb	-0.1	-0.1	0.05	0.18	0.44	0.036	-0.26	0.27	0.089	0.27	1	-0.0084	0.33	0.86	0.3	0.12
Te	0.065	0.043	0.03	0.032	0.01	-0.0073	0.041	0.0088	0.0026	0.031	-0.0084	1	0.04	-0.03	0.0041	0.0031
W	0.044	0.016	0.91	0.64	0.037	-0.0091	-0.043	-0.0097	0.031	0.027	0.057	0.065	0.032	-0.013	0.12	0.13
Pt	-0.17	-0.19	-0.022	0.05	0.0095	-0.033	-0.18	0.11	-0.031	-0.062	0.056	0.053	-0.091	0.049	-0.072	-0.062
Au	0.068	0.12	0.044	0.11	0.47	0.1	0.11	0.34	0.19	0.48	0.33	0.04	1	0.36	0.48	0.17
Tl	-0.071	-0.061	-0.0075	0.09	0.41	0.11	-0.2	0.27	0.11	0.28	0.86	-0.03	0.36	1	0.36	0.11
Pb	0.053	0.09	0.11	0.073	0.35	0.14	-0.05	0.16	0.41	0.47	0.3	0.0041	0.48	0.36	1	0.31
Bi	0.13	0.13	0.1	0.063	0.14	0.093	0.078	0.069	0.13	0.2	0.12	0.0031	0.17	0.11	0.31	1

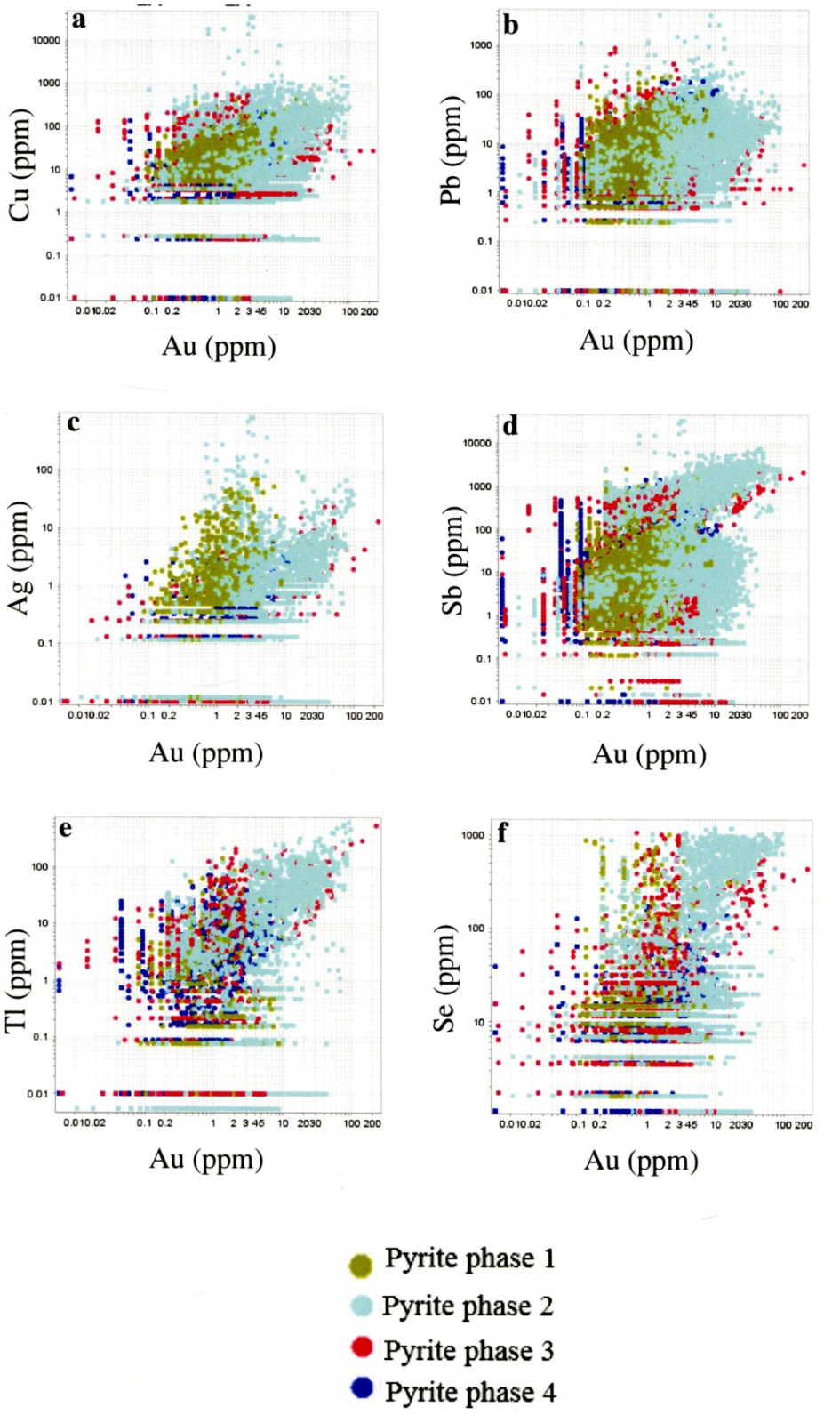

Figure 17. Binary plots show relationships of Au with Cu, Pb, Ag, Sb, Tl, and Se in the Tersang gold deposit, Malaysia. (a) Au vs Cu. (b) Au vs Pb. (c) Au vs Ag. (d) Au vs Sb. (e) Au vs Tl. (f) Au vs Se.

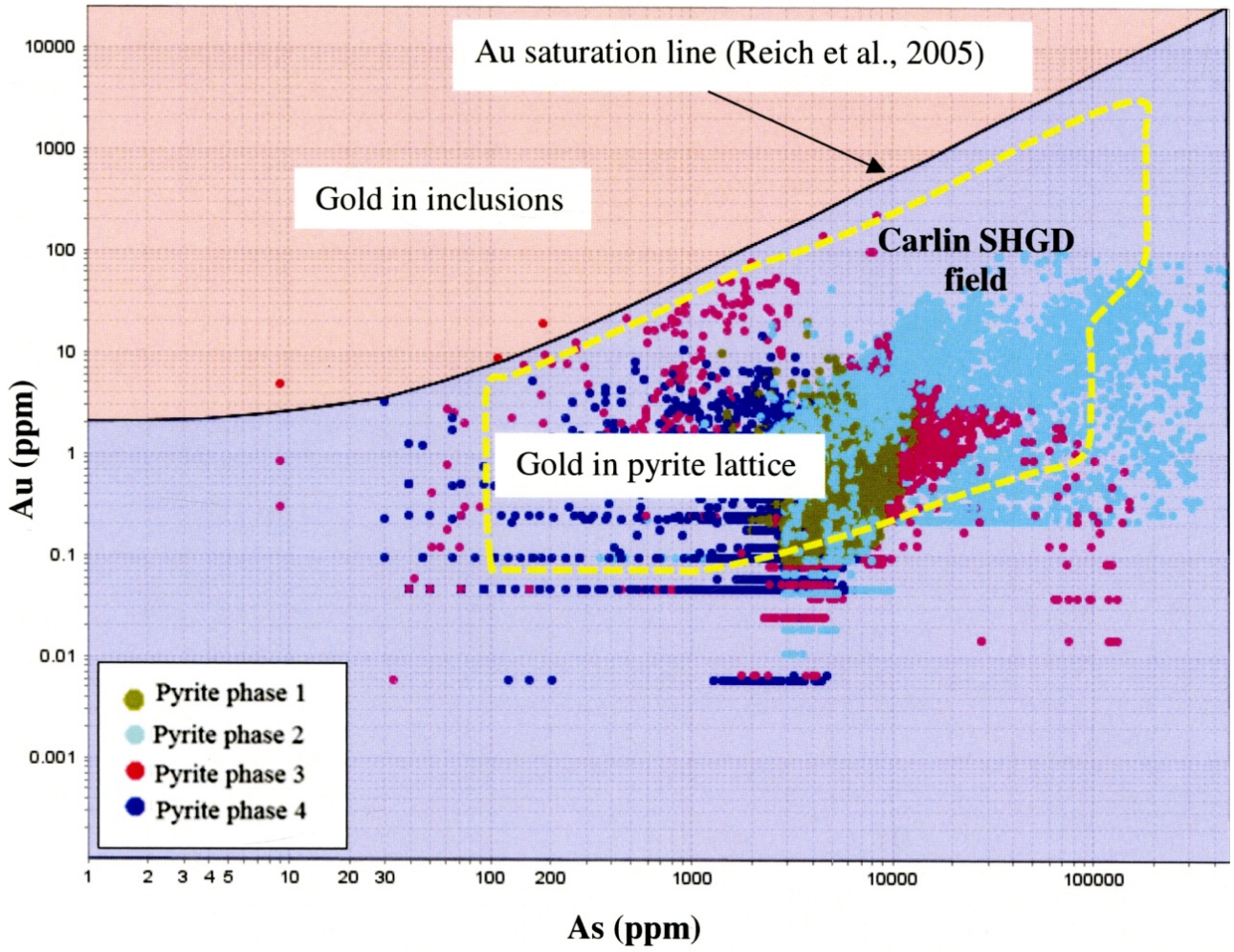

Figure 18. Gold solubility diagram adapted from Reich et al. (2005) showing relationship of Au and As. Pyrite phase 1 data mostly plot within the Carlin Sediment-hosted gold deposit (SHGD) field, whereas data of pyrite phases 2, 3, and 4 are scattered across the SHGD field. Pyrite phase 3 shows the existence of gold nanoparticles (free gold) above the Au saturation line.

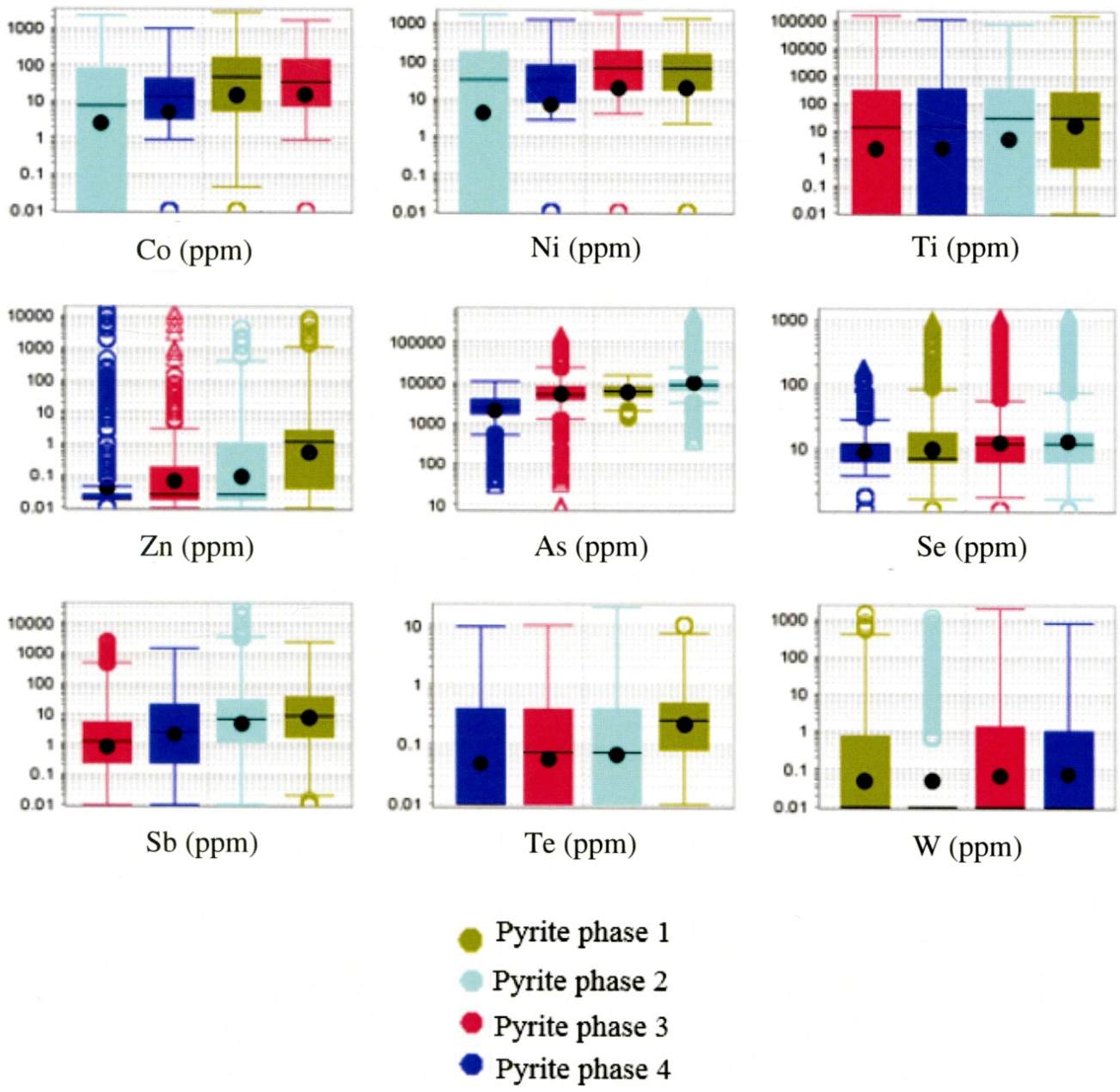

Figure 19. Box plot showing distribution of trace elements Co, Ni, Ti, Zn, As, Se, Sb, Te, and W in pyrite phases in the Tersang gold deposit, Malaysia. In the plot, the black circle represents the mean values (black circle), the line (or bar) is the median, the open circle is an outlier (top and bottom 5% of the data), the triangle the far outlier (highly anomalous value), and the central box represents 25 to 75 percentile of data (interquartile range) from Q1 and Q3. Q1 is the top of box and Q3 is the bottom of box. Whiskers are drawn to the last data point that extends 1.5 times the length of the box toward the maximum and minimum.

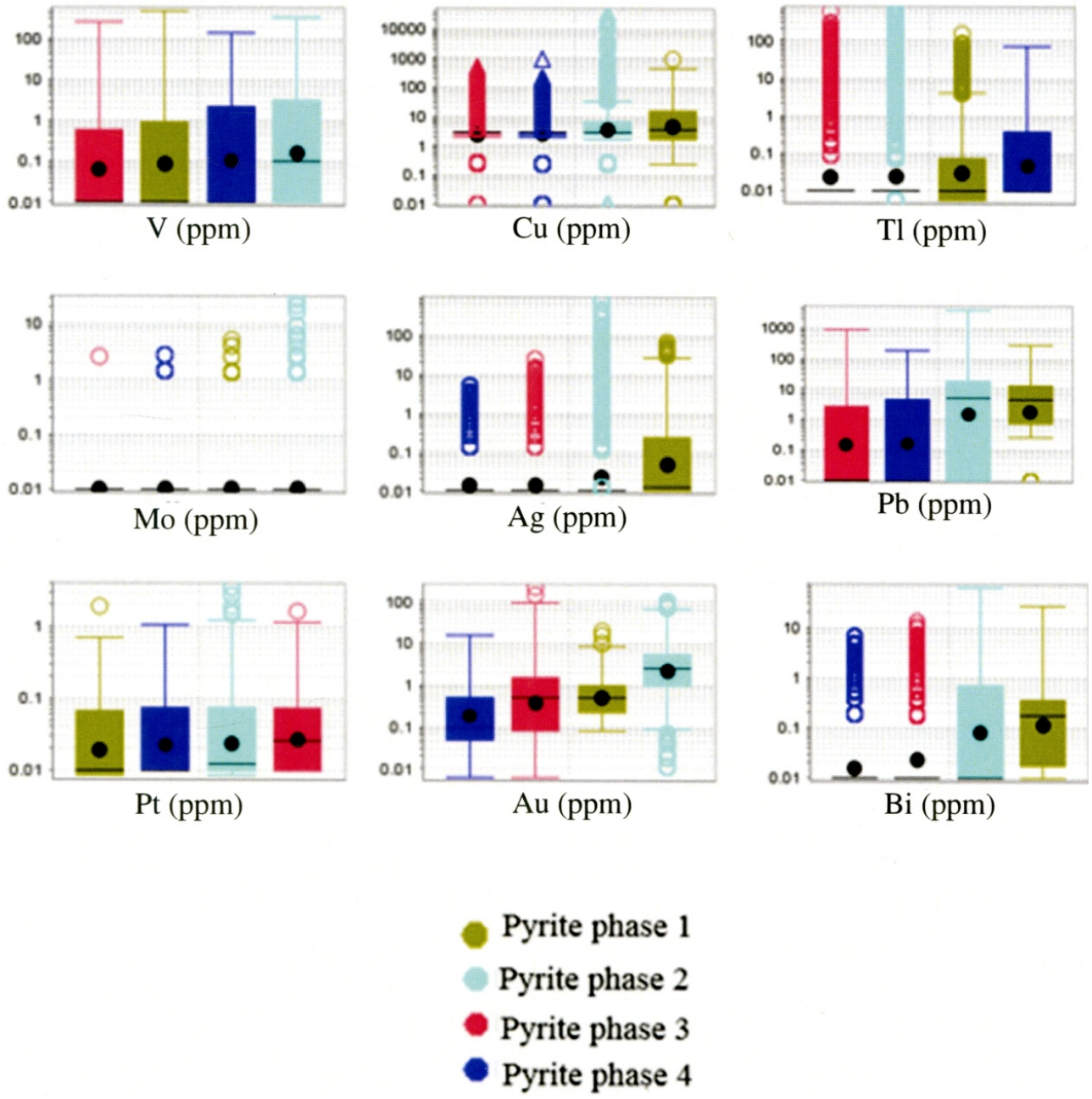

Figure 20. **Box plot showing distribution of trace elements V, Cu, Tl, Mo, As, Pb, Pt, Au, and Bi in pyrite phases in the Tersang gold deposit, Malaysia. In the plot, the black circle represents the mean values (black circle), the line (or bar) is the median, the open circle is an outlier (top and bottom 5% of the data), the triangle the far outlier (highly anomalous value), and the central box represents 25 to 75 percentile of data (interquartile range) from Q1 and Q3. Q1 is the top of box and Q3 is the bottom of box. Whiskers are drawn to the last data point that extends 1.5 times the length of the box toward the maximum and minimum.**

The maximum depositional age of the host sandstone (333.5 ± 2.5 Ma) at Tersang approximates the age of the host tuffaceous siltstone (331.3 ± 4.2 Ma) in the nearby Selinsing gold deposit [2].

The significance of the U-Pb zircon age is that the age is closer to the tuffaceous siltstone in the Selinsing gold deposit (further north), implying provenance of this zircon population from volcanic activities that produced the tuffaceous siltstone, further north, in the Selinsing area. Again, the maximum depositional age of 319.3 ± 5.3 Ma for the sandstone in the Tersang gold deposit is close to the Mississippian age of the host siltstone (324.1 ± 3.5 Ma) in the Selinsing gold deposit located further north of the Tersang gold deposit [2].

Most detrital zircon that were dated from the host sandstone and rhyolite are euhedral to subhedral and show a texture of oscillatory zoning implying an igneous origin of the zircon grains as most Th/U values are above 0.1. The zircon detritus may have derived from the N-S trending plutons belonging to the Main Range granites of peninsular Malaysia. The breccia was likely formed during faulting event that post-dated rhyolite emplacement and it is interpreted to be a tectonic breccia. This is consistent with the field observation showing the NE-SW trending breccia outcrop cross-cutting the rhyolite outcrop. Regionally, the evidence indicates that both the Tersang and Selinsing gold deposits [2] contain Carboniferous host rocks which are associated with Triassic magmatism.

9. Conclusion

LA-ICP-MS on pyrite from the host sandstone indicates variation in gold content across all pyrite phases at the Tersang gold deposit. Our LA-ICPMS trace element investigations have established that pyrite phases 2 and 3 have the highest gold levels. The significance of the U-Pb zircon age is that the age is closer to the tuffaceous siltstone in the Selinsing gold deposit (further north), implying provenance of this zircon population from volcanic activities that produced the tuffaceous siltstone, in the Selinsing area. Trace element composition of pyrite in the host sandstone indicates that Au positively correlates with As, Ag, Cu, Se, Sb, Pb and Tl in pyrite. These trace metals can be used as indicators for proximity to ore in the Tersang mineral district for orogenic-style gold mineralisation in Malaysia.

Acknowledgements

The authors would like to thank support from Peninsular Gold Limited and CODES Industry Project “Ore Deposits of SE Asia Project” led by Khin Zaw, University of Tasmania. Our thanks also go to Christine Cook and Karsten Goemann at the Central Science Laboratory, University of Tasmania for scanning electron microscope analysis. Many thanks go to Dr. Chun Kit Lai for his critical review and Dr. Sebastien Meffre for assistance in handling the LA-ICPMS dataset.

Conflict of Interest

All authors declare no conflicts of interest in this paper.

References

1. Richardson JA (1939) The Geology and mineral resources of the neighbourhood of Raub, Pahang, Federated Malay States, with an account of the Geology of the Raub Australian Gold Mine. Geological Survey Department, Federated Malay States, Memoir 3: 166.
2. Makoundi C, Khin Zaw, Large RR, et al. (2014) Geology, geochemistry and metallogenesis of the Selinsing gold deposit, central Malaysia. *Gondwana Res* 26: 241-261.
3. Metcalfe I (2011) Tectonic framework and Phanerozoic evolution of Sundaland. *Gondwana Res* 19: 3-21.
4. Metcalfe I (2012) Cold Gondwana to warm Tethys: Late Paleozoic-Mesozoic evolution of Tibetan and SE Asian continental blocks. 2012 IAGR Annual Convention and 9th International Symposium on Gondwana to Asia, Adelaide, Australia.
5. Oliver G, Khin Zaw, Hotson Mark, et al. (2014) U-Pb zircon geochronology of Early Permian to Late Triassic rocks from Singapore and Johor: a plate tectonic reinterpretation. *Gondwana Res* 26: 132-143.
6. Khin Zaw, Meffre S, Lai C-K, et al. (2014) Tectonics and metallogeny of mainland southeast Asia - a review and contribution. *Gondwana Res* 26: 1-4.
7. Yeap EB (1993) Tin and gold mineralisation in peninsular Malaysia and their relationships to the tectonic development. *J Southeast Asian Earth Sci* 8: 329-348.
8. Scrivenor JB (1928) The geology of Malayan ore deposits. Macmillan, London, 216.
9. Metcalfe I (2013) Tectonic evolution of the Malay Peninsula. J Asian Earth Sci 76: 195-213.
10. Kobayashi T, Tamura M (1968) Myophoria in Malaya with a note on the Triassic Trigoniacea. In: Kobayashi, T and Toriyama, R (Eds), Geology and palaeontology of Southeast Asia, University of Tokyo Press, 5: 88-137.
11. Makoundi C (2004) Facies analysis of the Triassic Jelai Formation in the Central Basin of Peninsular Malaysia: Implications on Paleogeography and Tectonics. MSc thesis, University of Malaya, 140.
12. Gobbett DJ, Hutchison CS (Eds) (1973) Geology of the Malay Peninsula: West Malaysia and Singapore. New York: Wiley-Interscience, 438.
13. Tan BK (1984) The Tectonic framework and evaluation of the Central Belt and its margin, Peninsular Malaysia. *Geological Society of Malaysia*. *Bulletin* 17: 307-322.
14. Metcalfe I (2002) Permian Tectonic Framework and Paleogeography of SE Asia. *J Asian Earth Sci* 20: 551-566.
15. Schwartz MO, Rajah SS, Askury AK, et al. (1995) The southeast Asian tin belt. *Earth Sci Rev* 38: 95-293

16. Bignell JD, Snelling NJ (1977) K-Ar ages on some basic igneous rocks from peninsular Malaysia and Thailand. *Bull Geol Soc Malays* 8: 89-93.
17. Metcalfe I (2000) The Bentong-Raub Suture Zone. *J Asian Earth Sci* 18: 691-712.
18. Kosler J (2001) Laser-ablation ICPMS study of metamorphic minerals and processes. *Mineral Assoc Can Short Course Handb* 29: 185-202.
19. Large RR, Danyushevsky L, Hollit C, et al. (2009) Gold and trace element zonation in pyrite using a laser imaging technique: implications for the timing of gold in orogenic and Carlin-style sediment-hosted deposits: *Econ Geol* 104: 635-668.
20. Danyushevsky LV, Robinson P, Gilbert S, et al. (2011) Routine quantitative multi-element analysis of sulphide minerals by laser ablation ICP-MS: Standard development and consideration of matrix effects. Geochemistry: Exploration, Environment, And Analysis 11: 51-60.
21. Wiendenbeck M, Alle P, Corfu F, et al. (1995) Three Natural zircon standards for U-Th-Pb, Lu-Hf, trace-element and REE analyses. *Geostand Newsl* 19: 1-23.
22. Black LP, Kamos L, Allen CM, et al. (2003) TEMORA 1. A new zircon standard for Phanerozoic U-Pb geochronology. *Chem Geol* 200: 155-170.
23. Jackson SE, Pearson NJ, Griffin WL, et al. (2004) The application of laser ablation inductively coupled plasma-mass spectrometry to in situ U-Pb zircon geochronology. *Chem Geol* 211: 47-69.
24. Black LP, Gulson BL (1978) The age of the Mud Tank Carbonatite, Strangways Range, Northern Territory. *BMR J Aust Geol Geophys* 3: 227-232.
25. Black LP, Kamo SL, Allen CM, et al. (2004) Improved 206Pb/238U microprobe geochronology by the monitoring of a trace-element related matrix effect; SHRIMP, ID-TIMS, ELA-ICP-MS, and oxygen isotope documentation for a series of zircon standards. *Chem Geol* 205: 115-140.
26. Meffre S, Large RR, Scott R, et al. (2008) Age and pyrite Pb-isotopic composition of the giant Sukhoi Log sediment-hosted gold deposit, Russia. *Geochimt Cosmochim Acta* 72: 2377-2391.
27. Paton C, Woodhead JD, Hellstrom JC, et al. (2010) Improved laser ablation U-Pb zircon geochronology through robust down-hole fractionation correction. *Geochem Geophys Geosyst* 11: 1525-2027.
28. Rumsey DJ (2016) Statistics For Dummies. 2nd Edition, Wiley Brand, 48.
29. Haile NS, Stauffer PH, Krishnan D, et al. (1977) Paleozoic redbeds and radiolarian chert: reinterpretation of their relationships in the Bentong and Raub areas, West Pahang, peninsular Malaysia. *Geol Soc Malays Bull* 8: 45-60.
30. Hoskin PWO, Schaltegger U (2003) The composition of zircon and igneous and metamorphic petrogenesis. *Rev mineral geochem* 53: 27-62.
31. Chun-Kit Lai, Meffre S, Crawford AJ, et al. (2014) The Central Ailaoshan ophiolite and modern analogues. *Gondwana Res* 26: 75-88.
32. Large RR, Bull SW, Maslennikov VV (2011) A carbonaceous sedimentary source-rock model for Carlin-type and orogenic gold deposits. *Soc Econ Geol* 106: 331-358.

33. Kolker A, Cannon WF, Westjohn DB, et al. (1998) Arsenic-rich pyrite in the Mississippian Marshall Sandstone: source of anomalous arsenic in southeatern Michigan ground water. *Geol Soc Am Abstr Progr* 30: A-59.
34. Kolker A, Goldhaber MB, Hatch JR, et al. (1999) Arsenic-rich pyrite in coals of the Warrior Field, northwestern Alabama: mineralogical evidence for a hydrothermal origin. *Geol Am Abstr Progr* 31: A-402.
35. Reich M, Kesler SE, Utsunomiya S, et al. (2005) Solubility of gold in arsenian pyrite. *Geochem Cosmochim Acta* 69: 2781-2796.
36. Goh KC (2013) Geological setting and mineralisation characteristics of the sedimentary rock hosted disseminated Jugan Au deposit, Bau mining district, Sarawak, Malaysia. BSc (Honours) thesis, University of Tasmania, 94.

AIMS Press